

Prospects for the measurement of ν_μ disappearance at the FNAL–Booster

The NESSiE Collaboration

Abstract

Neutrino physics is nowadays receiving more and more attention as a possible source of information for the long-standing problem of new physics beyond the Standard Model. The recent measurement of the mixing angle θ_{13} in the standard mixing oscillation scenario encourages us to pursue the still missing results on leptonic CP violation and absolute neutrino masses. However, puzzling measurements exist that deserve an exhaustive evaluation.

The NESSiE Collaboration has been setup to undertake conclusive experiments to clarify the *muon–neutrino disappearance* measurements at small L/E , which will be able to put severe constraints to models with more than the three-standard neutrinos, or even to robustly measure the presence of a new kind of neutrino oscillation for the first time.

To this aim the use of the current FNAL–Booster neutrino beam for a Short–Baseline experiment has been carefully evaluated. This proposal refers to the use of magnetic spectrometers at two different sites, Near and Far. Their positions have been extensively studied, together with the possible performances of two OPERA–like spectrometers. The proposal is constrained by availability of existing hardware and a time–schedule compatible with the CERN project for a new more performant neutrino beam, which will nicely extend the physics results achievable at the Booster.

The possible FNAL experiment will allow to clarify the current ν_μ disappearance tension with ν_e appearance and disappearance at the eV mass scale. Instead, a new CERN neutrino beam would allow a further span in the parameter space together with a refined control of systematics and, more relevant, the measurement of the antineutrino sector, by upgrading the spectrometer with detectors currently under R&D study.

A. Anokhina¹¹, A. Bagulya¹⁰, M. Benettoni¹², P. Bernardini^{8,7}, R. Brugnera^{13,12}, M. Calabrese⁷, A. Cecchetti⁶, S. Cecchini³, M. Chernyavskiy¹⁰, P. Creti⁷, F. Dal Corso¹², O. Dalkarov¹⁰, A. Del Prete⁹, G. De Robertis¹, M. De Serio^{2,1}, L. Degli Esposti³, D. Di Ferdinando³, S. Dusini¹², T. Dzhatdov¹¹, C. Fanin¹², R. A. Fini¹, G. Fiore⁷, A. Garfagnini^{13,12}, S. Golovanov¹⁰, M. Guerzoni³, B. Klicek¹⁵, U. Kose⁵, K. Jakovic¹⁵, G. Laurenti³, I. Lippi¹², F. Loddo¹, A. Longhin⁶, M. Malenica¹⁵, G. Mancarella^{8,7}, G. Mandrioli³, A. Margiotta^{4,3}, G. Marsella^{8,7}, N. Mauri⁶, E. Medinaceli^{13,12}, A. Mengucci⁶, R. Mingazheva¹⁰, O. Morgunova¹¹, M. T. Muciaccia^{2,1}, M. Nessi⁵, D. Orecchini⁶, A. Paoloni⁶, G. Papadia⁹, L. Paparella^{2,1}, L. Pasqualini^{4,3}, A. Pastore¹, L. Patrizii³, N. Polukhina¹⁰, M. Pozzato^{4,3}, M. Roda^{13,12}, T. Roganova¹¹, G. Rosa¹⁴, Z. Sahnoun^{3‡}, S. Simone^{2,1}, C. Sirignano^{13,12}, G. Sirri³, M. Spurio^{4,3}, L. Stanco^{12,a}, N. Starkov¹⁰, M. Stipcevic¹⁵, A. Surdo⁷, M. Tenti^{4,3}, V. Togo³, M. Ventura⁶ and M. Vladymyrov¹⁰.

(a) Spokesperson

1. INFN, Sezione di Bari, 70126 Bari, Italy
 2. Dipartimento di Fisica dell'Università di Bari, 70126 Bari, Italy
 3. INFN, Sezione di Bologna, 40127 Bologna, Italy
 4. Dipartimento di Fisica dell'Università di Bologna, 40127 Bologna, Italy
 5. European Organization for Nuclear Research (CERN), Geneva, Switzerland
 6. Laboratori Nazionali di Frascati dell'INFN, 00044 Frascati (Roma), Italy
 7. INFN, Sezione di Lecce, 73100 Lecce, Italy
 8. Dipartimento di Matematica e Fisica dell'Università del Salento, 73100 Lecce, Italy
 9. Dipartimento di Ingegneria dell'Innovazione dell'Università del Salento, 73100 Lecce, Italy
 10. Lebedev Physical Institute of Russian Academy of Science, Leninskie pr., 53, 119333 Moscow, Russia.
 11. Lomonosov Moscow State University (MSU SINP), 1(2) Leninskie gory, GSP-1, 119991 Moscow, Russia
 12. INFN, Sezione di Padova, 35131 Padova, Italy
 13. Dipartimento di Fisica e Astronomia dell'Università di Padova, 35131 Padova, Italy
 14. Dipartimento di Fisica dell'Università di Roma "La Sapienza" and INFN, 00185 Roma, Italy
 15. Rudjer Boskovic Institute, Bijenicka 54, 10002 Zagreb, Croatia
- ‡ Also at Centre de Recherche en Astronomie Astrophysique et Geophysique, Alger, Algeria

Contents

1	Introduction and Physics overview	5
2	Beam evaluation and constraints	8
2.1	The Booster Neutrino Beam (BNB)	8
2.2	The Far-to-Near ratio (FNR)	8
2.3	Systematic Uncertainties on the FNR	12
2.4	Monte Carlo beam simulation	12
2.5	Choice of the experimental sites	13
2.5.1	Dependence on the detector position of ν_μ CC rates and energy spectra	13
2.5.2	Systematics in the Far-to-Near ratio for a set of detector configurations.	17
2.6	Conclusions for the Booster Beam	24
3	Spectrometer Design Studies	26
4	Scintillator target at the Near site	30
5	Monte Carlo Detector Simulation and Reconstruction	33
5.1	Simulation	33
5.2	Reconstruction	35
6	Mechanical Structure	40
7	Magnet Power Supply and Slow Control	43
7.1	Power Supply features	43
7.2	Monitored quantities for every magnet	43
7.3	The Slow Control System	44
8	Detectors for the Iron Magnets	45
8.1	RPC Detectors	45
8.2	Detector Ancillary Systems	45
8.3	The Tracking Detectors for the Near and Far Spectrometers	46
8.4	RPC Production and Quality Controls	46
8.5	Costs	46
9	Backgrounds	47
9.1	Uncorrelated Background	47
9.2	Cosmic Ray Background	47
10	Read-out, Trigger and DAQ	48
10.1	DAQ overview	48
10.2	Data Flow	49
10.3	Front-End- Electronics	49
10.4	DAQ	50

11 FNAL Logistics, Schedule and Costs	51
11.1 Schedule and Costs	53
12 Physics Analysis and Performances	55
12.1 Standard Sensitivity Analysis	59
12.2 Full simulation and Matrix–Correlation	61
12.2.1 Observables spectrum evaluation	61
12.2.2 Results	63
12.3 Profile CLs	68
13 Conclusions	72

1 Introduction and Physics overview

The unfolding of the physics of the neutrino is a long and exciting story spanning the last 80 years. Over this time the interchange of theoretical hypotheses and experimental facts has been one of the most fruitful demonstrations of the progress of knowledge in physics. The work of the last decade and a half finally brought a coherent picture within the Standard Model (SM) (or some small extensions of it), namely the mixing of three neutrino flavour states with three ν_1 , ν_2 and ν_3 mass eigenstates. The last unknown mixing angle, θ_{13} , was recently measured [1, 2, 3, 4] but still many questions remain unanswered to completely settle the scenario: the absolute masses, the Majorana/Dirac nature and the existence and magnitude of leptonic CP violation. Answers to these questions will beautifully complete the (standard) three-neutrino model but they will hardly provide an insight into new physics Beyond the Standard Model (BSM). Many relevant questions will stay open: the reason for neutrinos, the relation between the leptonic and hadronic sectors of the SM, the origin of Dark Matter and, overall, where and how to look for BSM physics. Neutrinos may be an excellent source of BSM physics and their story is supporting that at length.

There are actually several experimental hints for deviations from the “coherent” picture described above. Many unexpected results, not statistically significant on a single basis, appeared also in the last decade and a half, bringing attention to the hypothesis of the existence of *sterile neutrinos* [5]. We refer to a White Paper [6], which contains a comprehensive review of these issues. We also refer to the very recent discovery of B-modes in the polarization pattern of the Cosmic Microwave Background by BICEP-2 [7] and its possible implication for sterile neutrinos (see e.g. [8] and references therein). In particular we would like to focus about tensions in many phenomenological models that grew up with experimental results on neutrino/antineutrino oscillations at Short-Baseline (SBL) and with the more recent, carefully recomputed, antineutrino fluxes from nuclear reactors. The main source of tension corresponds to the lack so far of any ν_μ disappearance signal [9].

This scenario promoted several proposals for new, exhaustive evaluations of the neutrino behaviour at SBL. Since end 2012 CERN is undergoing a study to setup a Neutrino Platform, with a new infrastructure at the North Area that may eventually include a new neutrino beam [10]. Meanwhile FNAL is welcoming proposal of experiments to exploit the physics potentialities of their two existing neutrino beams. Two very recent proposals have been submitted for experiments of SBL at the Booster beam, to complement the soon starting of MicroBooNE [11]. The two proposals from the LAr1-ND [12] and the ICARUS [13] Collaborations are both based on the Liquid Argon technology and aim to measure the ν_e appearance at SBL, with some possibilities to study also the ν_μ disappearance.

The present proposal is based on the following considerations:

- the measurement of ν_μ behaviour is mandatory for a correct interpretation

of the ν_e data, even in case of a null result for the latter;

- a decoupled measurement of ν_e and ν_μ interactions will allow to keep at low level systematics due to the different cross-sections;
- very massive detectors are mandatory to collect a large number of events and therefore improve the disentangling of systematic effects.
- the current experimental knowledge of the ν_μ disappearance at SBL is limited by the dated CDHS experiment [14] and the more recent results from MiniBooNE [15], a joint MiniBooNE/SciBooNE analysis [16, 17] and MINOS [18]. The latter results slightly extend the ν_μ disappearance exclusion region by CDHS. Fig. 1 shows the excluded regions in the space parameters for the $\nu_\mu \rightarrow \nu_s$ oscillation, obtained through ν_μ disappearance experiments. The mixing angle is denoted as θ_{new} and the squared mass difference as Δm_{new}^2 . The region with $\sin^2(2\theta_{new}) < 0.1$ is largely still unconstrained.

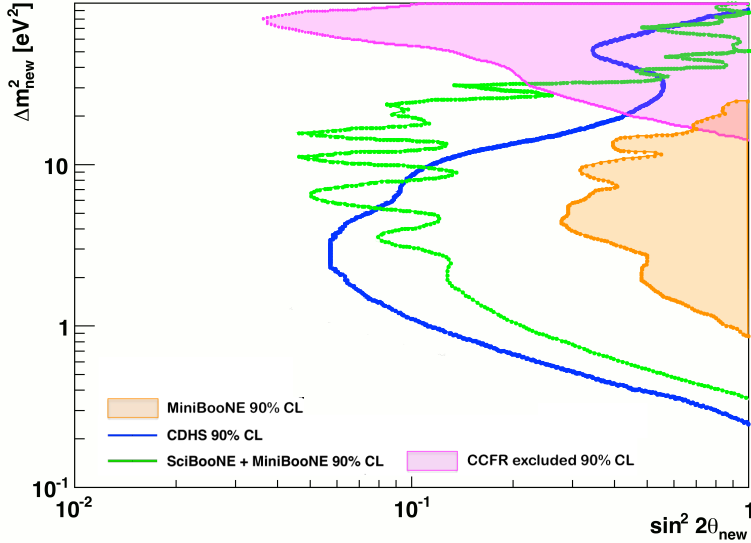


Figure 1: The current exclusion limits on the ν_μ disappearance searches at the eV^2 scale. Blue (green) line: old (recent) exclusion limits on ν_μ from previous CDHS [14] and recent MiniBooNE/SciBooNE [16, 17] measurements. The two filled areas correspond to the exclusion limits on the $\bar{\nu}_\mu$ from CCFR [19] and MiniBooNE-alone [15] experiments (at 90% C.L.).

Motivated by this scenario a detailed study of the physics case for the FNAL-Booster beam was performed. The study follows the similar analysis performed for the CERN-PS and CERN-SPS cases [20, 21] and the study in [22]. However, we tackled many specific detector configurations investigating experimental aspects not fully covered by the LAr detection. This includes the measurements of the lepton charge on event-by-event basis and its energy

over a wide range. Indeed, the muons from Charged Current (CC) neutrino interactions play an important role in disentangling different phenomenological scenarios provided their charge state is determined. Also, the study of muon appearance/disappearance can benefit of the large statistics of CC muon events from the primary neutrino beam. In the FNAL–Booster beam the antineutrino contribution is rather small and it then becomes a systematic effects to be taken into account.

Results of our study are reported in detail in this proposal. We aim to design, construct and install two spectrometers at each site, “Near” (110 m in line with the beam) and “Far” (710 m on surface), of the SBL FNAL–Booster, fully compatible with the already proposed LAr detectors. Profiting of the large mass of the two spectrometer–systems their stand–alone performances have been exploited for the ν_μ disappearance study. Besides, complementarity measurements with LAr can be undertaken to increase their control of systematic errors.

Some important practical constraints were assumed in order to draft the proposal on a conservative, manageable basis, and maintain it sustainable in terms of time–scale and cost. Well known technologies were considered as well as re–using large parts of existing detectors.

The momentum and charge state measurements of muons in a wide energy range, from few hundreds MeV/c to several GeV/c, over a $> 50 \text{ m}^2$ surface, is an extremely challenging task if constrained by an order of a million € budget for construction and installation. Running costs have to be kept at low level, too.

We believe to have succeeded to develop a substantial proposal that, by keeping the systematic error at the level of $1 \div 2\%$ for the measurements of the ν_μ interactions, will allow to:

- measure ν_μ disappearance in the almost entire available momentum range ($p_\mu \geq 500 \text{ MeV}/c$). This is a key information in rejecting/observing the anomalies over the whole expected parameter space of sterile neutrino oscillations, since the latter range drives the Δm_{new}^2 interval;
- collect a very large statistical sample to allow to span the oscillation mixing parameter up to till un–explored regions ($\sin^2(2\theta_{new}) \gtrsim 0.01$);
- measure the neutrino flux at the Near detector, in the relevant muon momentum range, to keep the systematic errors at the lowest possible values;
- measure the sign of the muon charge to separate ν_μ from $\bar{\nu}_\mu$ to control systematics.

In the next Section a detailed and exhaustive study using different simulations of the FNAL–Booster is reported, to work out a realistic choice for the detector configuration, and to correctly identify some sources of the systematic effects. In Sect. 3 the choice and the outlook of the spectrometers from OPERA [23] are discussed. After a brief discussion about the possibility to add a small target section (Sect. 4) to allow an on–site separation of CC and

neutral current (NC) events, the full details of the Monte Carlo simulation and reconstruction for neutrino events (Sect. 5) are illustrated. Sections 6 and 7 deal with the technical definition of the mechanical structure and electrical setting-up for the magnets. Sect. 8 illustrates the use of the already available detectors from OPERA. Sect. 9 debates about background levels to be taken into account for the data taking, which is described in Sect. 10. The following Section reports about FNAL setting-up, schedule and costs. The physics performances are extensively described in Sect. 12. To this regard several different approaches of the statistical methods to get the achievable sensitivities have been taken into account. Comprehensive discussions on the results have been outlined. Finally conclusions are recapped.

2 Beam evaluation and constraints

In this section we walked-through the exhaustive study on the characteristics of the FNAL-Booster ν_μ beam we underwent. Beam convolution with the muon detection systems described later was also carefully taken into account.

2.1 The Booster Neutrino Beam (BNB)

The neutrino beam [24] is produced using protons with a kinetic energy of 8 GeV extracted from the Booster and directed to a Beryllium cylindrical target with a length of 71 cm and a diameter of 1 cm. The target is surrounded by a magnetic focusing horn pulsed with a 170 kA current at a rate of 5 Hz. Secondary mesons are projected into a 50 m long decay pipe where they are allowed to decay in flight before being absorbed by an absorber and the ground material. An additional absorber can be placed in the decay pipe at about 25 m from the target^a. Neutrinos travel about horizontally at a depth of about 7 m underground.

Proton batches typically contain about 4.5×10^{12} protons. They have a duration of 1.6 μ s and are subdivided into 84 bunches. Bunches are about 4 ns wide and separated by about 19 ns. The rate of batch extraction is limited by the horn pulsing at 5 Hz. This timing structure provides a very powerful constraint to the background from cosmic rays.

2.2 The Far-to-Near ratio (FNR)

The uncertainty on the absolute ν_μ flux at MiniBooNE is shown in Fig. 2 (left) (from [24]). It stays below 20% for energies below 1.5 GeV while it increases drastically above that energy. The uncertainty is dominated by the knowledge of hadronic interactions of protons on the Be target, which modifies the angular

^aThis configuration, which is not currently in use, could eventually alter the beam properties (i.e. providing a more point-like source for the Near site) thus allowing for extra experimental constraints on the systematic errors.

and momentum spectra of neutrino parents emerging from the target. The result of Fig. 2 is based on experimental data obtained by the HARP and E910 collaborations.

This large uncertainty makes the use of two or more identical detectors at different baselines mandatory for the search of small disappearance phenomena. The ratio of the event rates at the Far and Near detectors as function of neutrino energy (FNR) is a convenient variable since it benefits at first order from cancellation of systematics due to the common effects of proton–target and neutrino cross–sections and the effects of reconstruction efficiencies.

Thanks to these cancellations the uncertainty on the FNR or, equivalently, on the Far spectrum extrapolated from the Near spectrum is usually at the percent level. As an example the uncertainty on FNR for the NuMI beam is shown in bins of neutrino energy in Fig. 2 (right) (from [25]). The uncertainty ranges in the interval 0.5–5.0%.

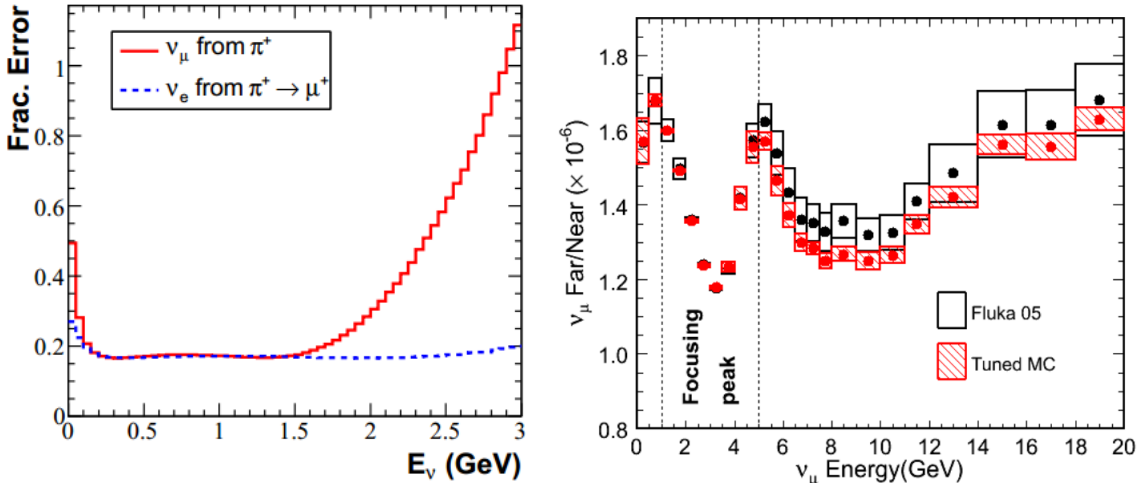


Figure 2: Left: uncertainties on the absolute flux of ν_μ at MiniBooNE; right: FNR at NuMI and the associated uncertainties given by box sizes; taken from [24] and [25], respectively.

It can be noted that, even in the absence of oscillations, the energy spectra in the two detectors are different, thus leading to a non–flat FNR. This is especially true if the distance of the Near detector is comparable to the length of the decay pipe. It is therefore essential to master the knowledge of the FNR for physics searches.

Compared to the Far site the solid angle subtended by the Near detector. Moreover neutrinos coming from meson decays at the end of the decay pipe have a higher probability of being detected. In the Far detector, on the contrary, only neutrinos produced in a narrow forward cone will be visible.

The effect of the increased acceptance of the Near detector for neutrinos from late decays is illustrated in Fig. 3. It is shown the ratio of the distributions of the neutrino production points (radius R vs longitudinal coordinate Z) for a sample crossing a Near and a Far detector placed at 110 and 710 m from

the target, respectively. Neutrinos produced at large Z can be detected in the Near detector even if they are produced at relatively large angles. This tends to enhance the low energy part of the spectrum. On the other hand neutrinos coming from meson decays late in the decay pipe are coming from the fast pion component which is more forward–boosted. The former effect is the leading one so the net effect is a softer energy spectrum at the Near site.

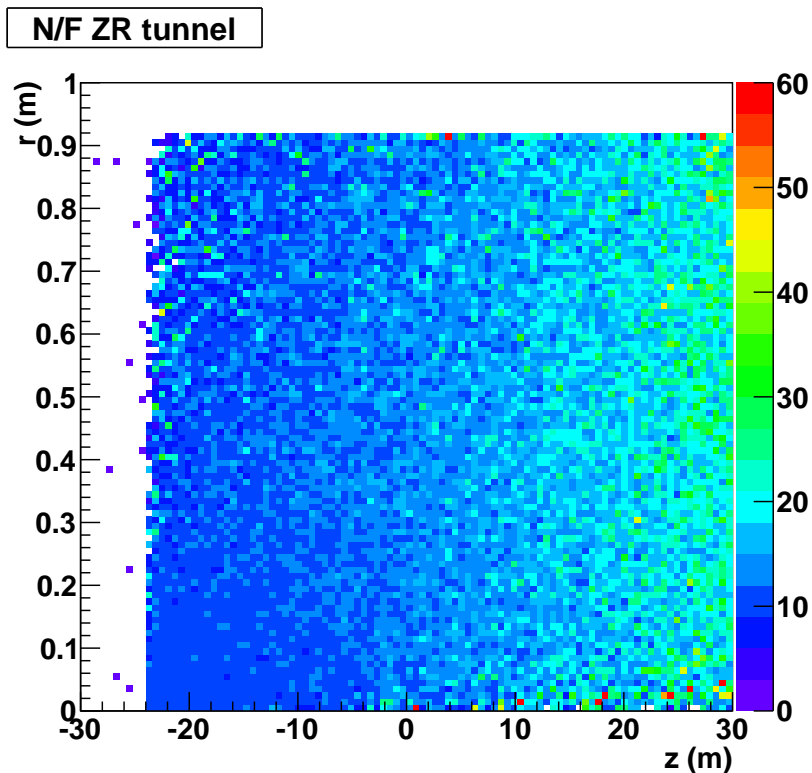


Figure 3: Ratio between the Z – R distributions of neutrino production points for neutrinos observed in a Near detector over neutrinos observed in a Far detector. Two effects are most relevant: there is no apparent dependence on the radial R distribution; and, as expected, the Near detector has a higher acceptance for neutrinos produced in the most downstream part of the decay pipe, i.e. at high Z .

The top plots of Fig. 4 show the distribution of E_ν vs Z for neutrinos crossing the Near (top left) and the Far site (top right). As anticipated, the energy spectrum at the Near site is softer, the additional contribution at low energy being particularly important for neutrinos coming from meson decays late in the decay pipe. The distribution of Z is also shown in Fig. 4 for neutrinos crossing the Near (bottom left) and Far site (bottom right).

From these qualitative considerations it becomes clear that the prediction of the FNR is a delicate task requiring a full simulation of the neutrino beamline and of the detector acceptance. We will now consider the sources of systematic uncertainties on the FNR.

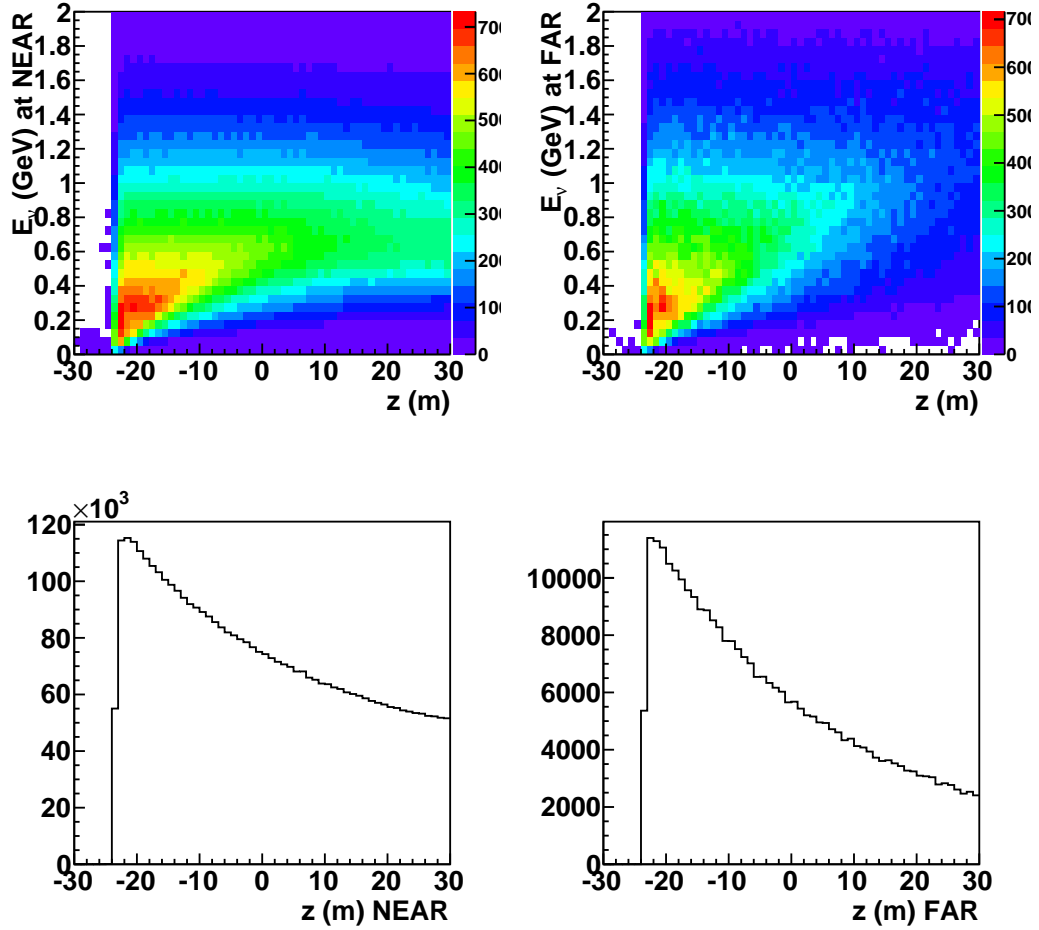


Figure 4: *Distribution of E_ν vs Z for neutrinos seen in the Near (top left) and Far (top right) detectors. Distribution of Z for neutrinos seen in the Near (bottom left) and Far (bottom right) detectors. The points at low energy and very Z are due to decays of pions emitted backward.*

source	% error
p -Be π^+ production	13.8%
2^{ry} nucleons interactions	6.2
p -delivery	2%
2^{ry} pions interactions	1.5
magnetic field	1.5%
beamline geometry	1%

Table 1: *Systematic uncertainties on the ν_μ BNB flux prediction. Taken from [24].*

2.3 Systematic Uncertainties on the FNR

All the contributions to the systematic uncertainties have been studied in detail by the MiniBooNE collaboration in [24]. The results are summarized in Tab. 1. The dominant contribution comes from the knowledge of the hadroproduction double differential (p, θ) cross-sections in 8 GeV p -Be interactions. At first order these contributions factorize out using a double site. Due to its importance we have here focused on the largest contribution.

2.4 Monte Carlo beam simulation

In order to understand the hadroproduction uncertainty impact on the knowledge of the FNR for the specific case of our experiment we have developed a new beamline simulation. The angular and momentum distribution of pions exiting the Be target have been simulated using:

- FLUKA 2011.2b [26],
- GEANT4 (v4.9.4 p02, QGSP 3.4 physics list),
- a Sanford-Wang parametrization determined from a fit of the HARP and E910 data sets in [24],

$$\frac{d^2\sigma}{dpd\Omega} = c_1 p^{c_2} \left(1 - \frac{p}{p_B - 1}\right) \exp\left(-\frac{p^{c_3}}{p_B^{c_4}} - c_5 \theta (p - c_6 p_B \cos^{c_7} \theta)\right) \quad (1)$$

p_B being the proton beam momentum in GeV/c.

For the propagation and decays of secondary mesons a simulation using GEANT4 libraries has been developed. A simplified version of the geometry, which was derived from the literature, was adopted. Despite the approximations a fair agreement with the official simulation of the MiniBooNE Collaboration [24] has been obtained. This tool is sufficient for the purpose of the site optimization that will be described in the following. In order to fully take into account finite-distance effects, fluxes and spectra are derived after extrapolating neutrinos up to the detector volumes without using weighing techniques. A total number of 7×10^8 protons on target (p.o.t.), 2.1×10^8 p.o.t. and 1×10^9 pions have been simulated with FLUKA, GEANT4 and Sanford-Wang parametrization, respectively.

Fig. 5 shows the spatial distributions of neutrinos at their production point in the decay pipe. From top left in clockwise order are shown: the distance from the axis (R), X vs Y coordinates^b, X , R vs Z , Z and X vs Z .

Fig. 6 shows the spatial distributions of neutrinos at a distance of 110 m from the target. The r.m.s. of the distribution is about 5 m. The projected coordinate is shown in the bottom plot of Fig. 6 with a Gaussian fit superimposed. This plot indicates that placing the Near detector on surface would severely limit the statistics (furthermore this would make the angular acceptance of the Far and Near detectors too different).

2.5 Choice of the experimental sites

By supposing to have already decided the geometry and mass of the detectors, several considerations influence the choice of the experimental sites location.

The ultimate figure of merit is the power of exclusion (or discovery) for effects induced by sterile neutrinos in a range of parameters as wide as possible in a given running time.

To achieve good performances an essential point is the reliability of the simulation of the spectra of neutrinos at the Near and Far sites. As soon as the detectors are further away from the target they “see” more similar spectra since the production region can be better approximated as a point-like source. This helps in reducing the systematic uncertainty. This point is further addressed in Sect. 2.5.2.

On the other hand increasing the distances introduces the loss in the collectable event sample and reduces the lever-arm for oscillation studies.

Coming to practical constraints we note that increasing the depth of detectors impacts considerably the civil engineering costs. Furthermore the space along the BNB beamline is already partially occupied by existing or proposed experimental facilities (SciBooNE/LAr1-ND, T150-Icarus, MiniBooNE, MicroBooNE, LAr1 and ICARUS).

2.5.1 Dependence on the detector position of ν_μ CC rates and energy spectra

Fig. 7 shows how the rates of ν_μ CC interactions (top) and their mean energy (bottom) depend on the position with respect to the proton target. The horizontal axis shows the distance from the target in the horizontal direction (Z) while the vertical axis contains the depth from the ground surface.

It can be seen that at about 700 m distance the rate and mean energy is barely affected when moving from an on-axis to an off-axis position. This observation supports the idea of putting the Far detector at surface thus reducing the experiment cost.

^bThe reference frame used here is such that Y points upward and Z is along the proton beam direction.

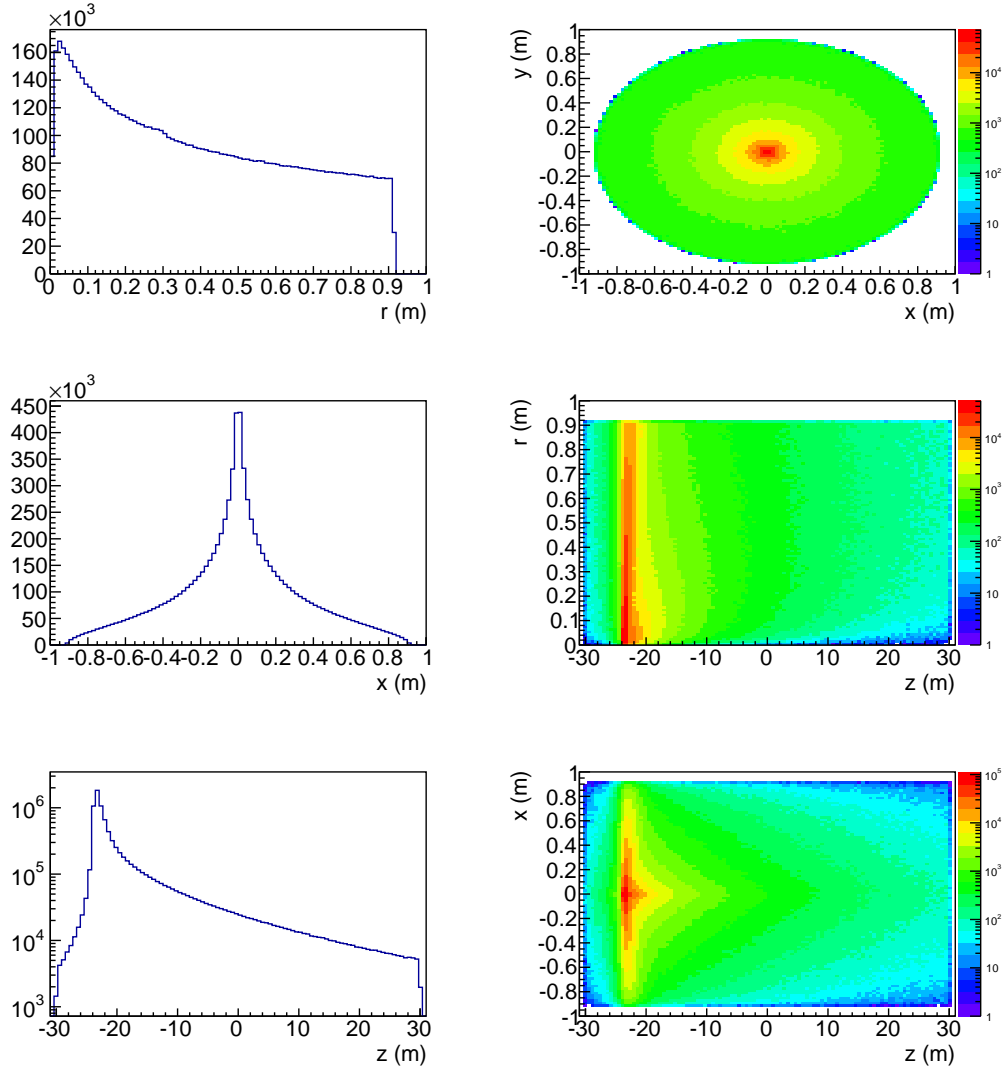


Figure 5: Distributions of the coordinates of neutrino production points in the decay pipe. Top left: radius. Top right: X vs Y . Middle left: X . Middle right: R vs Z . Bottom left: Z . Bottom right: X vs Z .

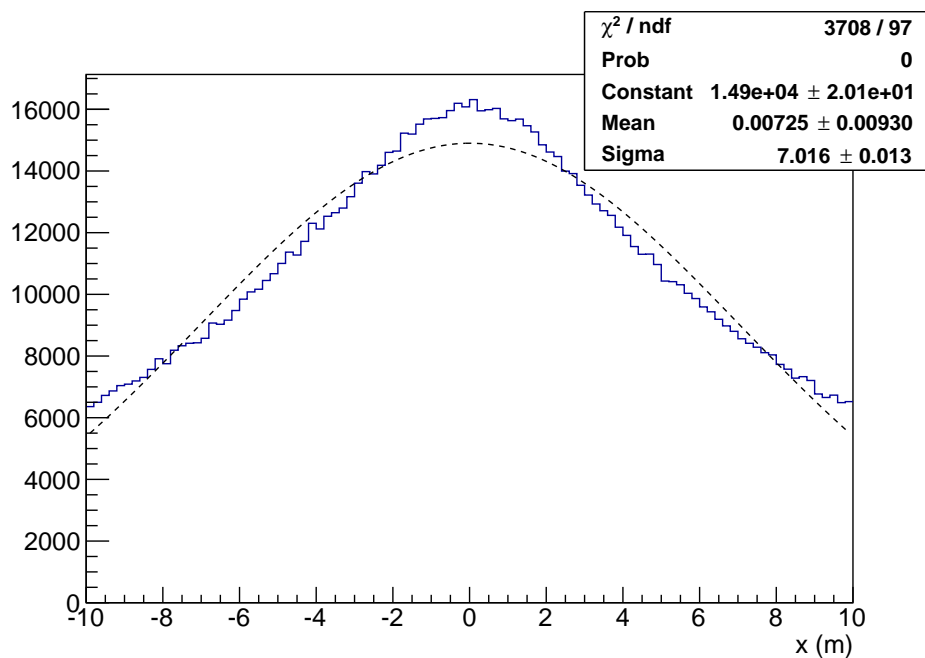
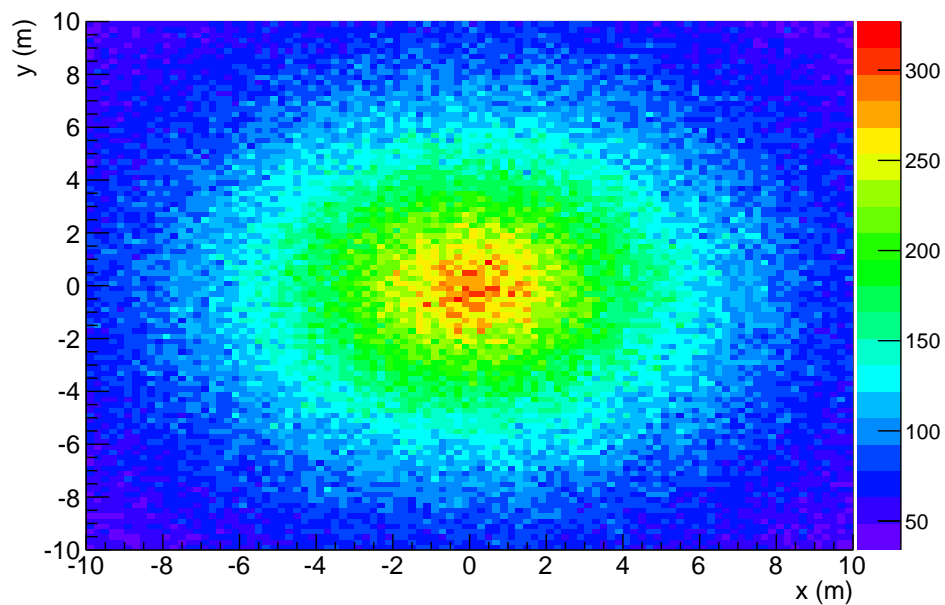


Figure 6: *Beam profile at 110 m from the target.*

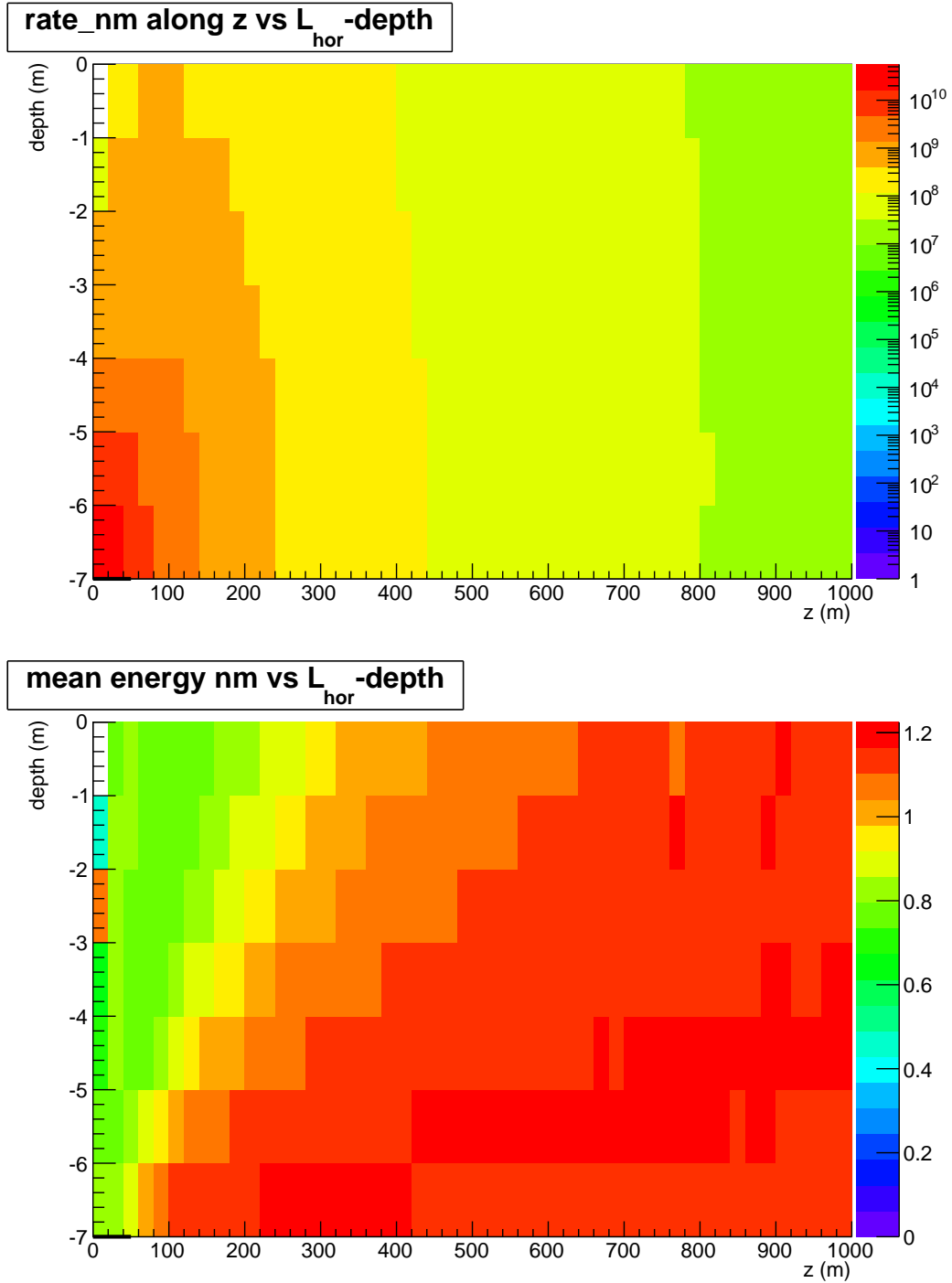


Figure 7: Top: ν_μ CC rate (a.u.) vs z and depth. Bottom: mean energy of ν_μ CC interactions (GeV) vs z and depth. The upstream side of the target is the origin of the reference system. The black line close to the origin represents the longitudinal extension of the decay pipe.

configuration	L_N (m)	L_F (m)	y_N (m)	y_F (m)	s_N (m)	s_F (m)
1	110	710	0	0	4	8
2	110	710	0	0	1.25	8
3	110	710	1.4	11	4	8
4	110	710	1.4	11	1.25	8
5	460	710	7	11	4	8
6	460	710	6.5	10	4	6

Table 2: Near–Far detectors configurations. $L_{N(F)}$ is the distance of the Near (Far) detector from the target. $y_{N(F)}$ is the vertical coordinate of the center of the fiducial area of the Near (Far) detector with respect to the beam axis which lies at about -7 m from the ground surface. $s_{N(F)}$ is the dimension of the fiducial area of the Near (Far) detector.

2.5.2 Systematics in the Far–to–Near ratio for a set of detector configurations.

A set of six configurations have been studied considering a combination of distances (110, 460 and 710 m), on–axis or off–axis configurations and different fiducial sizes of the detectors. Their geometrical parameters are given in Tab. 2 and illustrated schematically in Fig. 8.

- Configuration 1 considers two on–axis detectors at 110 and 710 m with squared active areas of 4×4 m² (Near) and 8×8 m² (Far). By selecting the subsample of neutrinos crossing the Near detector which are also crossing the Far detector, a well defined region is selected in the Near detector. This “shadow” (Fig. 9) is not sharp due to the fact that the source is not point–like.
- Configuration 2 uses a reduced Near detector area, limited to 1.25×1.25 m², chosen as such to increase the overlap of neutrinos seen in the two detectors.
- Configurations 3 and 4 replicate the same pattern as for 1 and 2 but having the Far detector at surface and the Near detector sharing the same off–axis angle (instead of both being on–axis).
- Configurations 4 and 5 are similar to 3 and 4 but for a more distant the Near site (460 m).

The FNRs for the six considered configurations using either FLUKA, GEANT4 or the Sanford–Wang parametrization for the simulation of p –Be interactions are shown in Fig. 10. The error bars here only indicate the uncertainty introduced by the limitations in Monte Carlo samples.

Configuration 1 (with on–axis detectors and a large Near detector) produces a FNR increasing with energy as expected from the considerations presented above and largely departing from a flat curve. By restricting the fiducial volume in the Near detector (configuration 2) the FNR flattens as expected. This behavior is also confirmed using off–axis detectors (configurations 3 and 4).

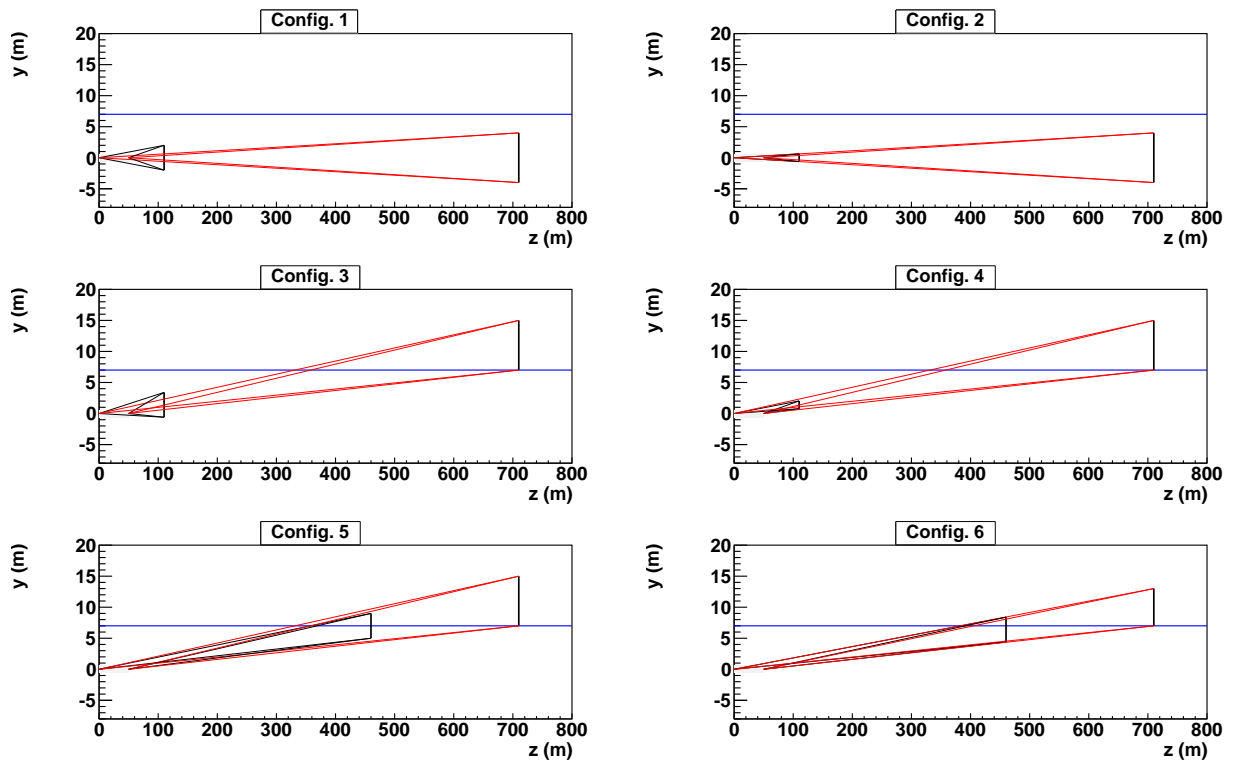


Figure 8: Configurations of Far and Near detectors in the $Y-Z$ plane (see also Tab. 2). The blue horizontal line marks the ground level, the vertical black lines mark the detectors and the red lines show the angle subtended by the detectors at the beginning and the end of the decay pipe.

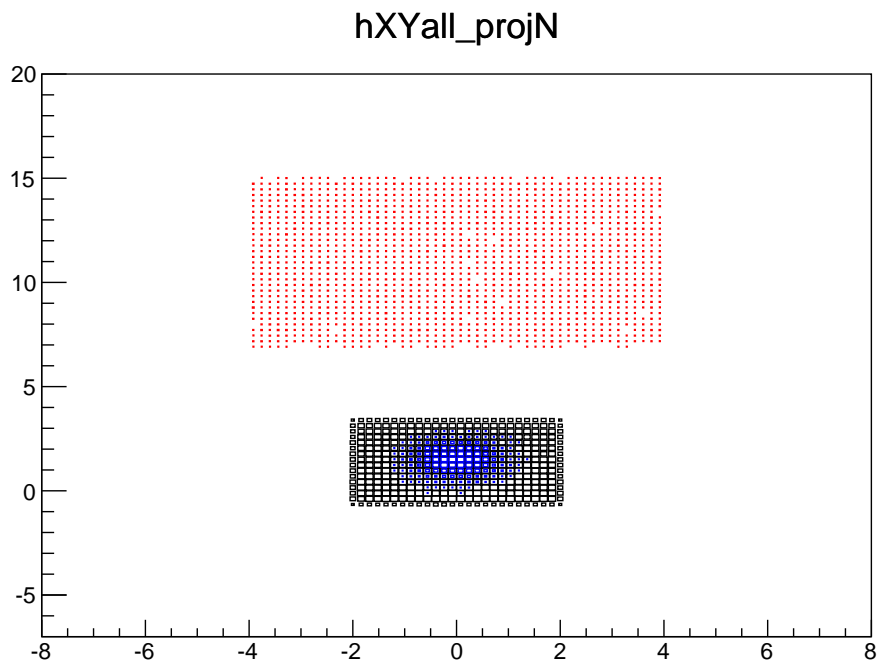


Figure 9: *Distribution of the impact points of neutrinos at the Near (black) and Far (red) sites. Units are in meters. The blue histograms shows the same distribution for the subsample of neutrinos crossing both the Far and Near detectors. Here we consider configuration 3 (see Tab. 2).*

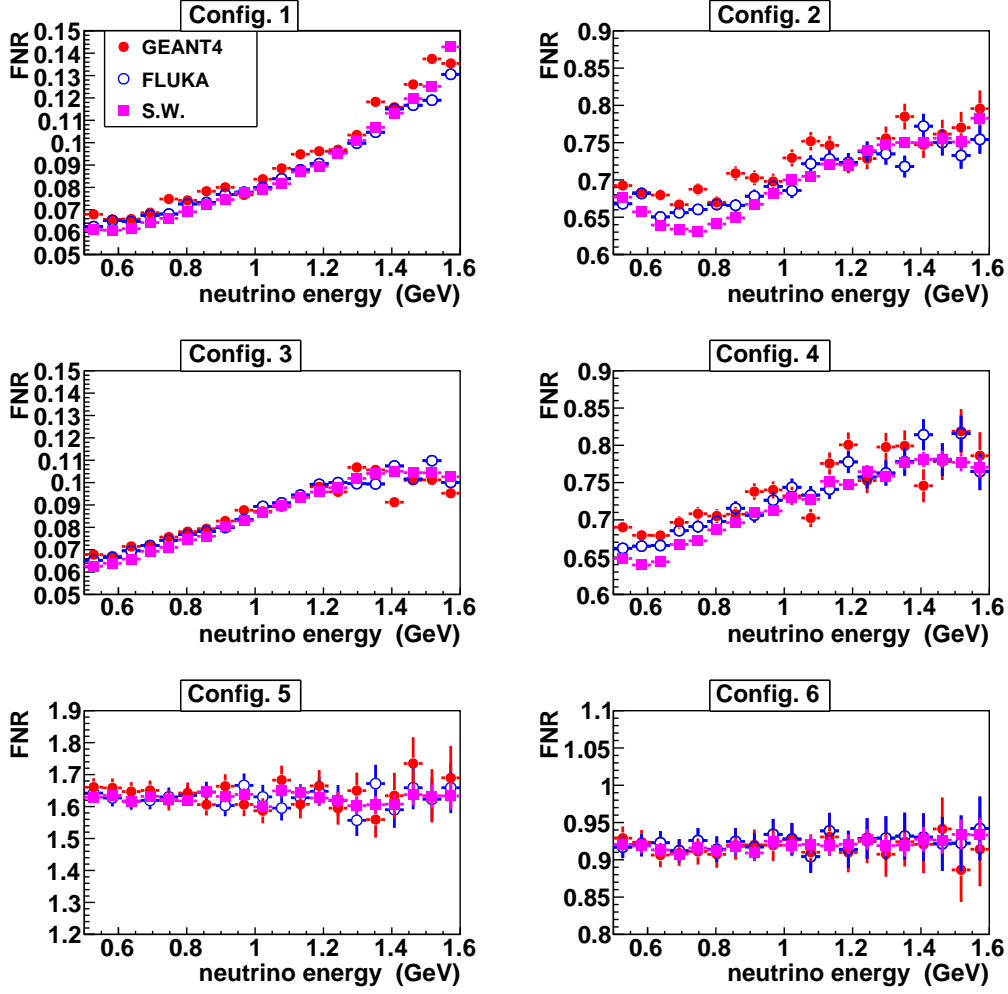


Figure 10: *Far-to-Near ratios for the six considered configurations. Comparison of FLUKA and GEANT4 for hadroproduction.*

Configurations with a Near detector at larger baselines (5 and 6) tend to produce quite flat FNRs, as expected.

The different behaviors are more easily visible in Fig. 11 where FNRs, normalized to each other, are compared (taking the Sanford–Wang parametrization).

We have used the differences in the hadronic models implemented in the FLUKA and GEANT4 generators to estimate the impact of the hadroproduction uncertainties on the FNR. The results are shown in Fig. 12 where we show the bin-by-bin ratios between the FNRs predicted by these two Monte Carlos for the six considered configurations. The yellow band visualizes the magnitude of a fixed 3% error on the FNR. It can be seen that the two simulations provide results which are in general in agreement at a level between 1 and 3% for configurations where the common region between the Far and Near detectors

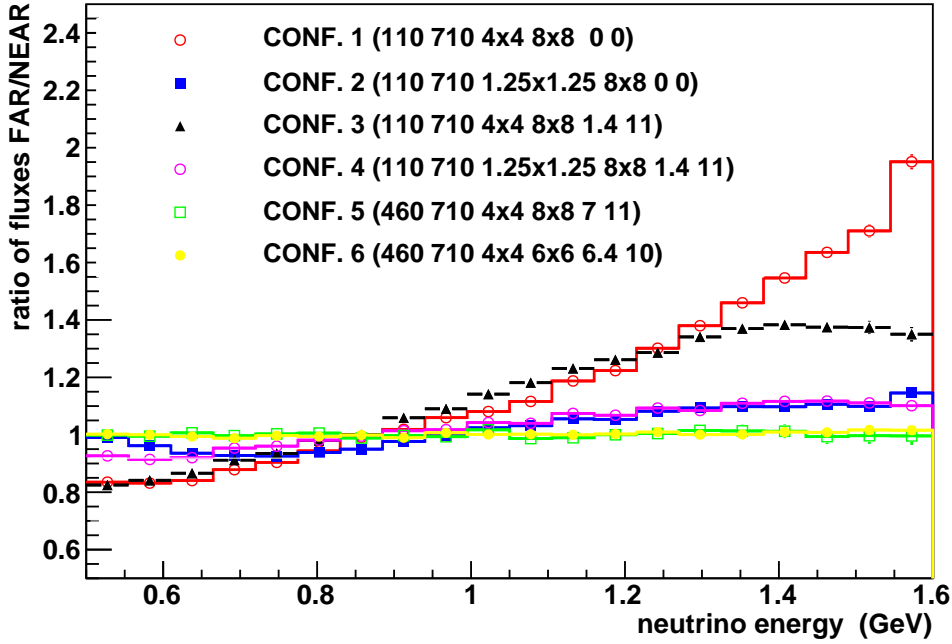


Figure 11: *Far-to-Near ratios for the six considered configurations using the Sanford-Wang parametrization.*

are considered.

Since specific hadroproduction measurements for the BNB Be target replica exist, a more appropriate way of addressing the hadroproduction related uncertainty on the FNR has also been adopted as follows. The coefficients c_i of the Sanford-Wang parametrization of pion production data from HARP and E910 in Eq. 1 have been sampled. Their correlations have been taken into account using the covariance matrix published in [24] and shown here in Fig. 13. The sampling of these correlated variables has been performed using the Cholesky decomposition of the covariance matrix. The correlation of the sampled variables reflects the information of the original covariance matrix as shown in Fig. 14.

For each sampling of the c_i coefficients, neutrinos have been weighted with a factor:

$$w(p_\pi, \theta_\pi) = \frac{\frac{d^2\sigma}{dpd\theta}(c_i)}{\frac{d^2\sigma}{dpd\theta}(c_i^0)} \quad (2)$$

depending on the momentum (p_π) and angle (θ_π) of their parent pion, c_i^0 being the best fit values of the fit to the HARP and E910 data sets. The resulting FNR ratios for a set of systematic variations of c_i are shown in Fig. 15 for the six considered configurations. Black bullets show the average value in each bin while error bars represent the r.m.s. of the samplings. Bottom plots (hollow bullets) in each configuration show the ratio of the r.m.s. over the central

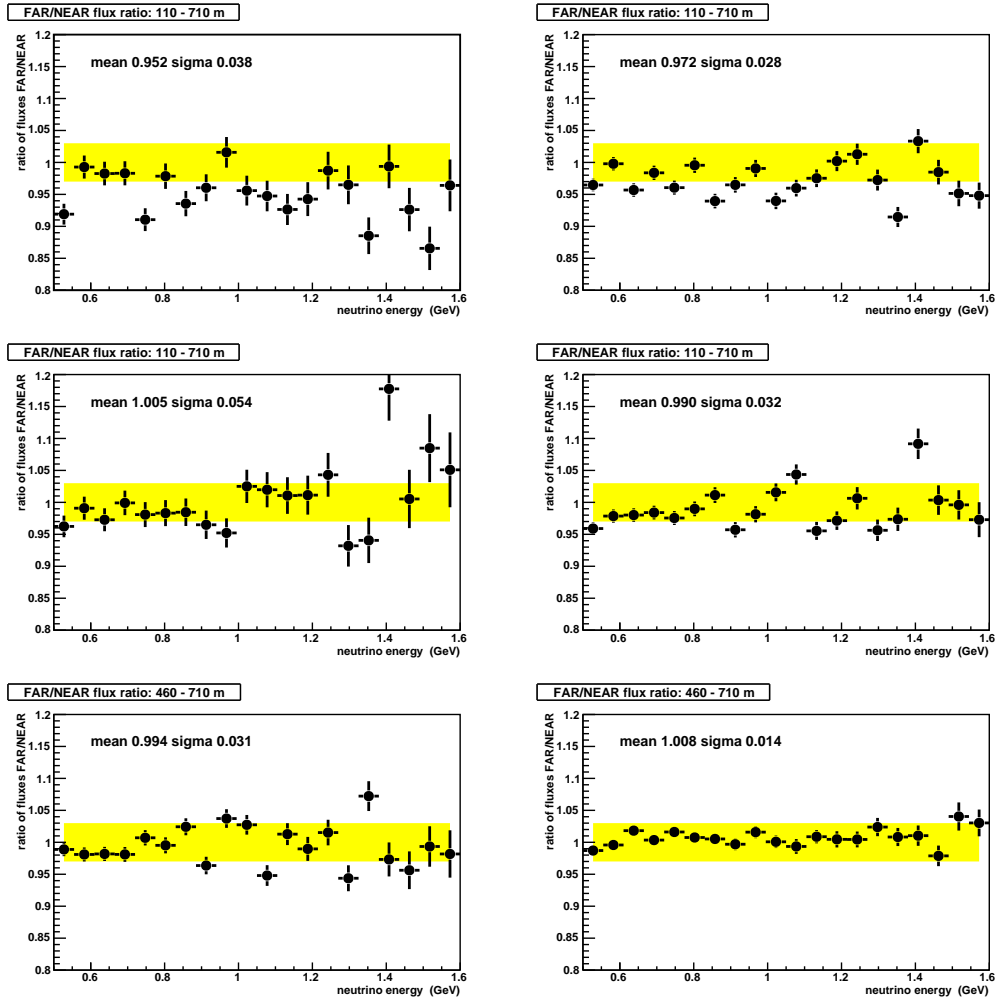


Figure 12: Comparison of FLUKA and GEANT₄ for hadroproduction.

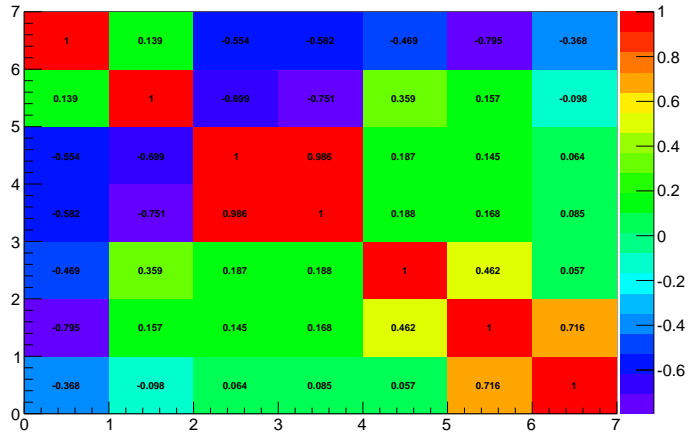


Figure 13: Covariance matrix of the c_i coefficients of the Sanford-Wang parametrization of pion production data from HARP and E910 in Eq. 1.

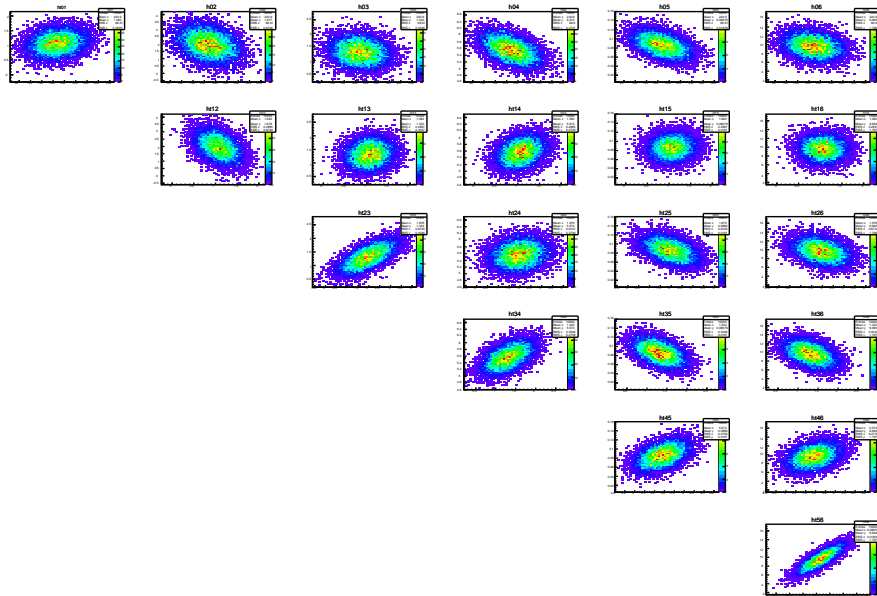


Figure 14: Correlation of the c_i parameters in Eq. 1.

value providing an estimate of the fractional systematic error. Uncertainties are rather large (5–7%) when taking the complete area of the Near detector at 110 m while they decrease significantly by restricting to the central region. In particular, configuration 4, which is realistic from practical considerations has an uncertainty ranging from 2% at low energy decreasing below 1.5% –0.5% for neutrino energies above 1 GeV. The uncertainty is also quite good (generally below 0.5%) for a Near site at 460 m.

2.6 Conclusions for the Booster Beam

Using the constraints from HARP/E910 data sets, we have estimated the uncertainties associated to hadroproduction the FNR being of order 1–2% for a configuration with the Far detector at surface and the Near detector with a similar off-axis angle and a fiducial volume tailored to match the acceptance of the Far detector (“configuration 4”). Given also the high available statistics and the large lever-arm for oscillation studied we consider such a layout with baselines of 110 m and 710 m as a viable choice. Of course, “configuration 4” is a subset of “configuration 3”, which could be that to be used in reality by rearranging the OPERA spectrometers (see next Section). Therefore, given the possibility for an higher statistics collection and the minor concern about the height of the pit (that has to be anyhow centered at the level of the beam) the following studies are driven by “configuration 3”.

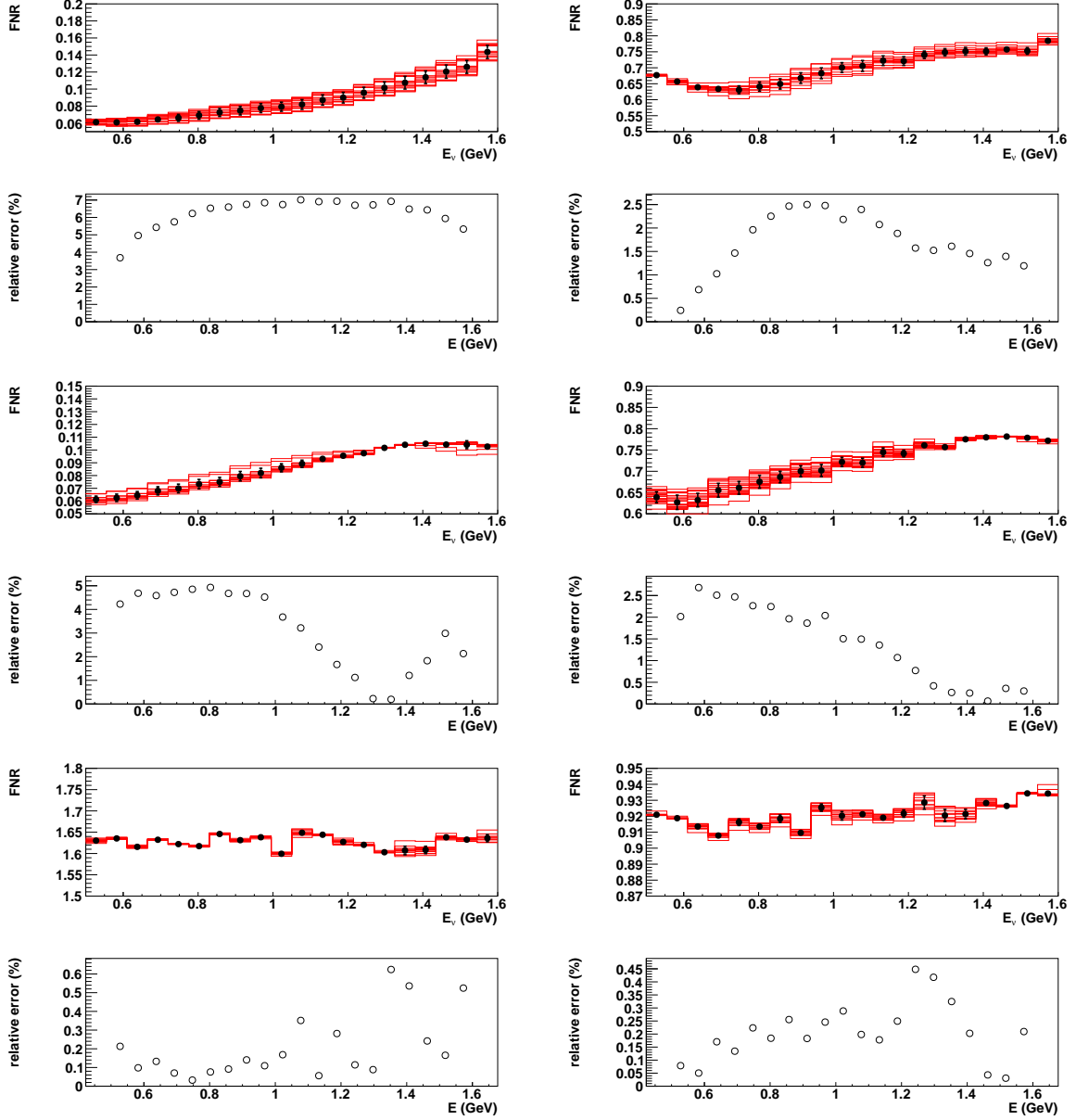


Figure 15: *Effect of data-driven hadroproduction uncertainties on the FNR calculated using the Sanford–Wang parametrization of for the six considered configurations. Red histograms show different samplings of the c_i parameters of Eq. 1. Black bullets show the average value in each bin while the error bars represent the r.m.s. of the samplings. Bottom plots (hollow bullets) in each configuration show the ratio of the r.m.s. over the central value giving an estimate of the fractional systematic error.*

3 Spectrometer Design Studies

The definition of two sites, Near and Far, constitutes a fundamental issue in the sterile neutrino search. Moreover the two detector systems at the two sites have to be as similar as possible. The NESSiE Far spectrometer has to be designed to cope with an aggressive time schedule and to largely exploit the acquired experience with the OPERA spectrometers in construction, assembling and maintenance [23]. Well known technologies have been considered as well as re-using large parts of existing detectors. The OPERA spectrometers will begin to be dismantled sometime next year and we foresee to use them totally. The relatively low momentum range of the muon tracks detected in the charged current events produced by the FNAL–BNB beam suggests to couple together the two OPERA spectrometers, either for the Far or the Near site. Their modularity will allow to take 4/7 of the acceptance region (in height) for the Far site and 3/7 for the Near one. Each iron slab (see Sect. 6) will be cut at 4/7 in height to reproduce exactly the Far and Near targets. In such a way any inaccuracy either in geometry (the single 5 cm iron slab owns a precision of few mm) or in the material will be exactly reproduced in the two detection sites. The Near NESSiE spectrometer will then be an exact clone of the Far one, with identical thickness along the beam but scaled transverse size.

The achievements of 5 cm slabs have been analyzed and compared with a possible more performant thickness.

The current OPERA spectrometer design with 5 cm iron slabs has been studied using a complete and detailed simulation, profiting from the technical knowledge acquired with OPERA. The detector simulation is organized in two steps: the first one is the particle propagation inside the apparatus, based on GEANT3.21, with the concurrent creation of track hits; the second one is the digitization, i.e. the detector response to track hits creating detector digits. At this level, the Resistive Plate Chamber (RPC) efficiencies are implemented in the Monte Carlo simulation, taking into account the different widths of the horizontal and vertical sets of read-out strips.

The achievements of the current geometry with 5 cm iron slabs are evaluated in terms of NC contamination and momentum resolution, and compared to a possible geometry with 2.5 cm slab thickness.

Using the current geometry with 5 cm iron slabs, the fraction of neutrino interactions in iron giving a signal in the RPCs ($\varepsilon \equiv \frac{(\geq 1RPC)}{all}$) is 68%. The efficiency for CC and NC separately is $\varepsilon_{CC} = 86\%$ and $\varepsilon_{NC} = 20\%$. This corresponds to a fraction of NC interactions over the total number of interaction $\frac{NC}{all} = 8.1\%$. With a minimal cut of 2 crossed RPC planes, the NC contamination is reduced to 4.2%; requiring 3 RPC planes the NC contamination is 3.0%. The distribution of crossed RPC planes is shown in Fig. 16 for both interaction channels, individually and jointly.

Using 2.5 cm thick slabs, the fraction of neutrino interactions giving a signal in the RPCs increases for both NC and CC events. The distribution of crossed RPC planes in this configuration is shown in Fig. 17. Both the efficiency ε_{CC} and the NC contamination are higher with respect to the reference 5 cm ge-

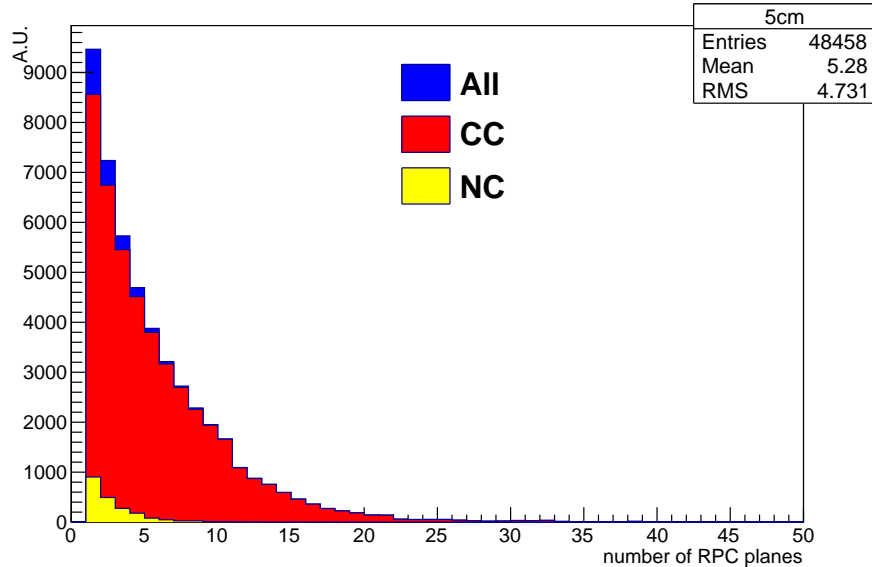


Figure 16: Number of crossed RPC planes with the 5 cm slab geometry.

ometry. In Fig. 18 the efficiency ε_{CC} and the purity $p \equiv \frac{CC}{all} = 1 - \frac{NC}{all}$ are shown as a function of the minimum number of crossed RPC planes for both slab thicknesses. It can be noted that for a given level of purity p the efficiencies for the two geometries are similar. No advantage in statistics is taken requiring the same NC contamination suppression.

The range in iron is reconstructed in three dimensions, merging the two RPC projection (horizontal and vertical) information. The muon momentum is obtained from the track range, using the continuous-slowing-down-approximation (CSDA) [28].

The muon momentum estimated in that way is compared to the true momentum in Fig. 19a and Fig. 19b for the two options, 5 cm and 2.5 cm, respectively. The resolution in either case is similar for the two considered geometries, even if the smaller thickness would allow a good evaluation at smaller momenta. The 5 cm option is however sufficient to allow estimation from the minimum momentum of 400 MeV/c or even lower (see also Sec. 5).

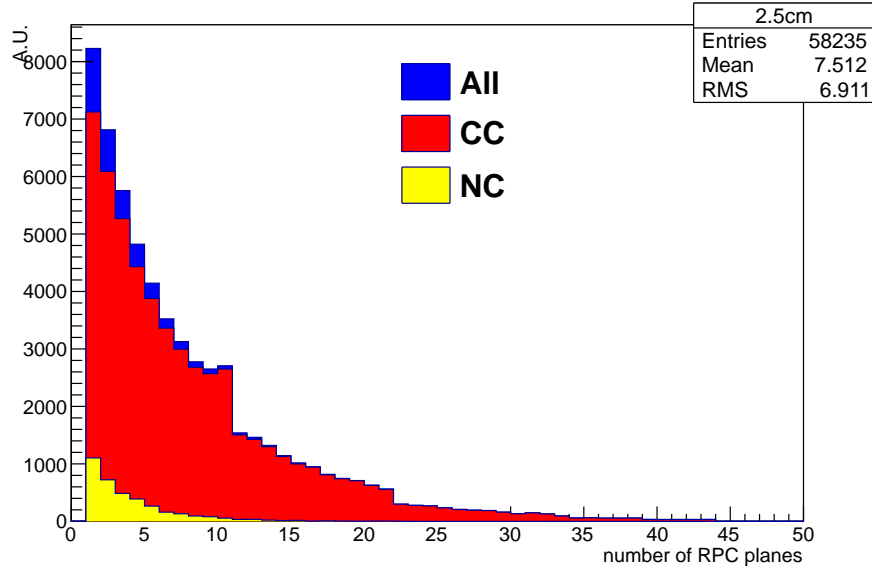


Figure 17: Number of crossed RPC planes with the 2.5 cm slab geometry. Note that the knee visible at 11 planes is due to the geometry of the OPERA spectrometers, which own a modularity of 11 detector-planes sandwiched into 12 iron slabs. This effect is present in any configuration but it comes more visible in the 2.5 cm case.

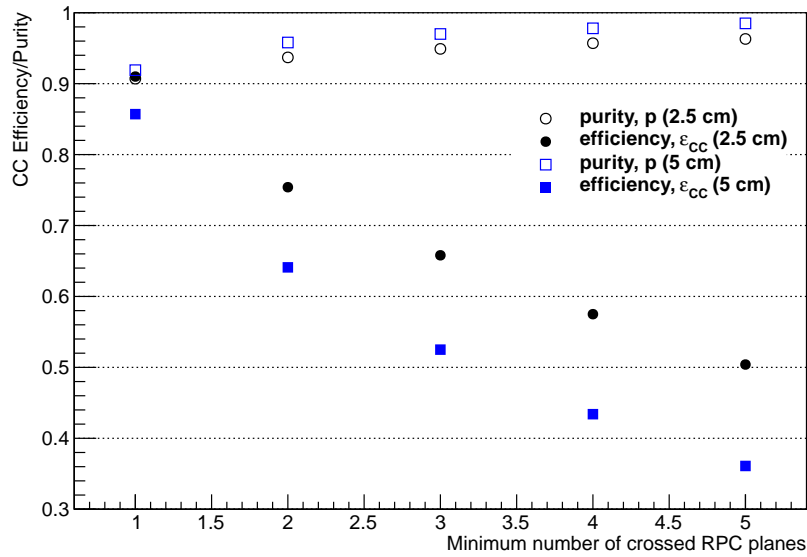
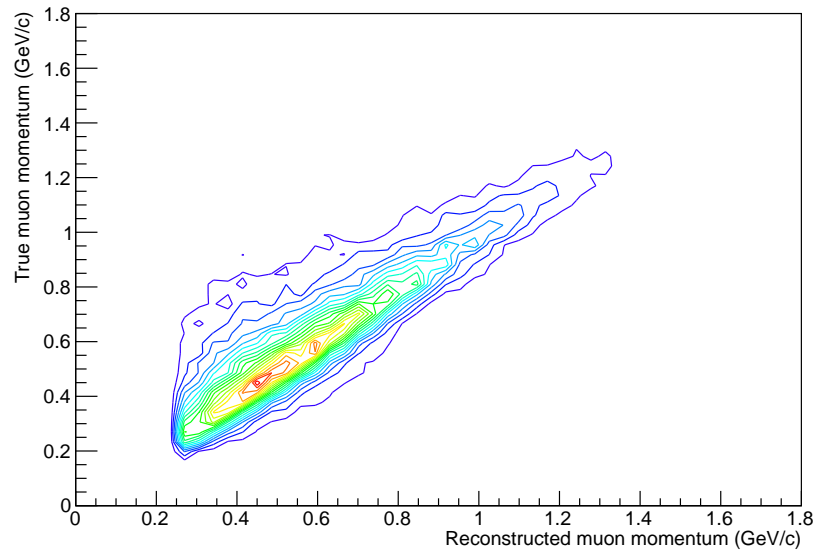
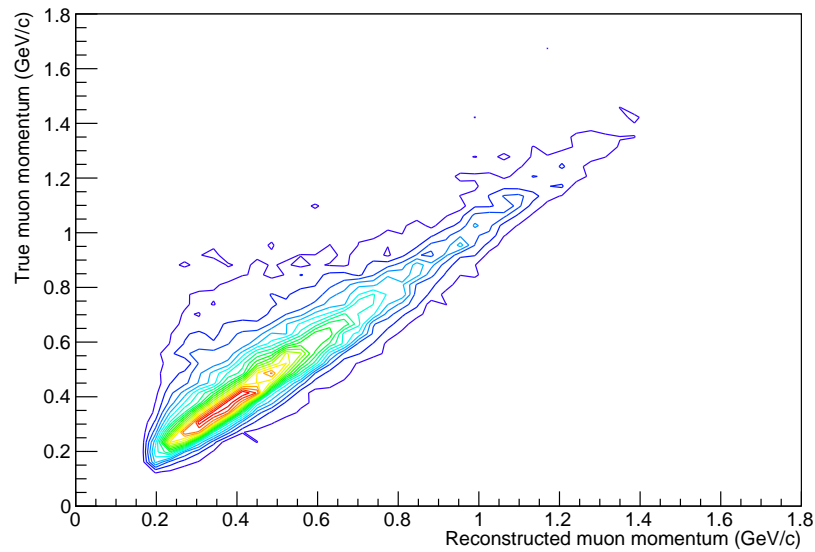


Figure 18: CC efficiency (ϵ_{CC} , points) and purity (p , open circles) as a function of the minimum number of RPC planes for the two spectrometer geometries, 5 cm slabs (in blue) and 2.5 cm slabs (in black). For a given level of purity p the efficiencies for the two geometries are similar, therefore no advantage in statistics is taken requiring the same NC contamination suppression.



(a) 5 cm iron slab



(b) 2.5 cm iron slab

Figure 19: True muon momentum as a function of the reconstructed muon momentum for the two geometries, 5 cm slabs (a) and 2.5 cm slabs (b). The second geometry would allow to extend the lower bound of the momentum measurement to 200 MeV at the expense of the level of CC purity. The 5 cm geometry will be able to reach anyhow the limit around 400 MeV keeping an high level of purity.

4 Scintillator target at the Near site

The Charged Current (CC) neutrino quasi-elastic (QE) scattering is the dominant process for neutrino interaction in the ~ 1 GeV region. In CCQE neutrino scattering the momentum of the produced lepton is strongly correlated with the energy of the neutrino. This implies that at these energies neutrino oscillations produce a distortion in the muon momentum spectrum similar to the one induced in the neutrino energy spectrum. Oscillation parameters (see Section 12.3) can also be extracted by fitting the muon momentum spectrum $\frac{dN}{dp_\mu}$ via the double ratio:

$$R = \frac{\left(\frac{\left(\frac{dN}{dp_\mu} \right)_{\text{Far}}}{\left(\frac{dN}{dp_\mu} \right)_{\text{Near}}} \right)_{\text{Data}}}{\left(\frac{\left(\frac{dN}{dp_\mu} \right)_{\text{Far}}}{\left(\frac{dN}{dp_\mu} \right)_{\text{Near}}} \right)_{\text{MC}}} \quad (3)$$

on the assumed oscillation model. For the double ratio it is important to have an accurate measurement of the neutrino CC interaction rate to constrain the MC predictions.

Moreover, as discussed in the previous Section, the contribution of neutral current (NC) events is limited at the low-momentum range and therefore it constitutes a systematic effect to deal with. Any measurement improving the disentanglement of NC and CC events will help in keeping that systematics under control. Other sub-leading effects may also exist, such as the contamination of muons coming from neutrino interactions in the rock and infrastructures surrounding the detectors, or even the possible appearance of the $\nu_\mu \rightarrow \nu_e$ “contamination”.

The study of these systematic effect can not rely only on MC simulations. Indeed neutrino interactions in the ~ 1 GeV region are mostly based on measurements of neutrino interactions on deuterium targets in bubble chambers [29]. In this energy region the nuclear effects of the neutrino target material (from Fermi motion and the nuclear potential) are significant, therefore cross-sections on deuterium target are not directly applicable to heavier nuclear target materials, like iron.

By an appropriate choice of an active target design, namely its mass and segmentation, a separation of the quasi-elastic part in the CC sample can also be attained. As a whole, that target would act as an independent detector to be used for inter-calibration and normalization of the different data samples.

To this end a plastic Scintillator Tracking Detector (STD) to be located at the Near site, upstream of the spectrometer, is under study. In its preliminary design it is formed by 20 Target Tracker Modules (TTMs), each composed of 1 cm thick iron slab followed by a Tracking Module (TM) section, based on the MINER ν A triangular scintillator bar technology [30]. An TM module consists of two planes of 64 scintillator bars, each 211 cm long with triangular cross-section (1.7 cm high and 3.3 cm side), and a central 2.6 mm diameter hole

to lodge the wavelength shifting (WLS) fiber (Fig. 20). Each bar is read by Silicon Photomultipliers (SiPM) with the hit position determined by analog pulse readout and analysis.

Scintillator bars have vertical or horizontal orientation to provide X and Y coordinates. Eight consecutive scintillator bi-planes with alternating orientation form a Tracking Module.

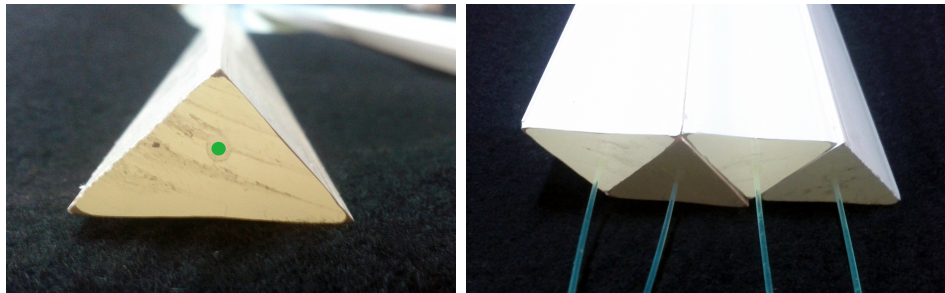


Figure 20: *Left: triangular scintillator bar and WLS fibers. Right: sketch of a 2 plane scintillator bar tracker.*

The STD allows an accurate tracking of particles emerging from the interaction down to low energy with a sufficient level arm to reconstruct the neutrino interaction vertex in the iron. Based on the track fine sampling the particle identification through dE/dx near the end point on stopping tracks can be obtained. A sketch of the possible detector configuration is shown in Fig. 21. Two scintillator planes with horizontal and vertical orientation with a larger cross-section with respect to the TTM is placed upstream would act as veto for neutrino interaction occurring outside the detector.

With a total iron target mass of ~ 7 tons the expected CC interaction rate is $\sim 2 \times 10^4 \nu_\mu \text{ CC}/10^{20} \text{ p.o.t.}$. According to references [31] and [32], with an integrated intensity of $2.2 \times 10^{20} \text{ p.o.t.}$ corresponding to 1 year of data taking, the ν_μ CC rate can be determined with a 3% accuracy and the NC/CC ratio with a precision better than 10%. A detailed Monte Carlo simulation is under development to precisely evaluate the detector performances. In the present document no further reference is made to this subdetector that, at the present stage, was only introduced as a possibility to be considered^c.

^cIn Tab. 7 where costs are given, a first estimation for this detector is anyhow provided.

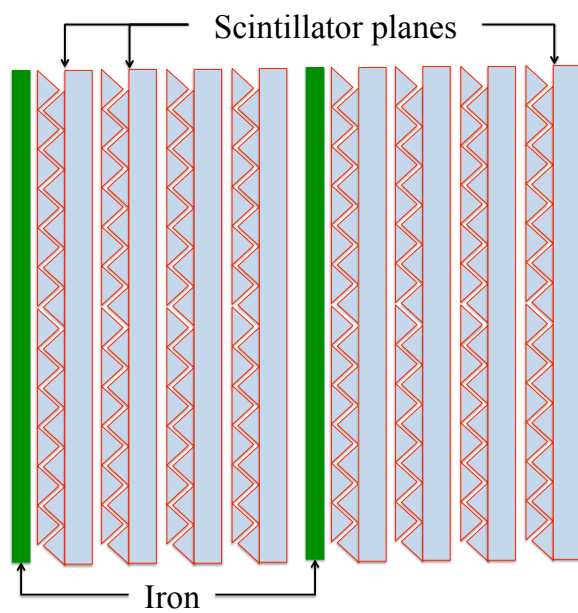


Figure 21: *Side view of two Target Tracker Modules.*

5 Monte Carlo Detector Simulation and Reconstruction

The present proposal has been extensively developed using full-detail programming and up-to-date software packages to obtain precise understanding of acceptances, resolutions and physics output. Although not all possible options have been studied, a rather exhaustive list of different magnet configurations and detector designs has been adopted as benchmark for further studies once the detector structure will be finalized.

5.1 Simulation

The aim of the simulation of the apparatus is to help the design studies reported here and to understand the main features of the proposed experiment. The simulated detector consists of a Near and Far magnetic spectrometer (ND and FD, respectively). The muon neutrino and antineutrino Booster fluxes for positive and negative beam polarity were considered, with a beam of 0 mrad tilted with respect to the horizontal.

Neutrino interactions are generated in the Iron target using GENIE [27] with standard parameters and including all interaction processes (QE, RES, DIS, NC), as shown in Fig. 22. Distribution of particles in the hadronic systems are shown in Fig. 23; muon momentum and angle in Fig. 24 and 25.

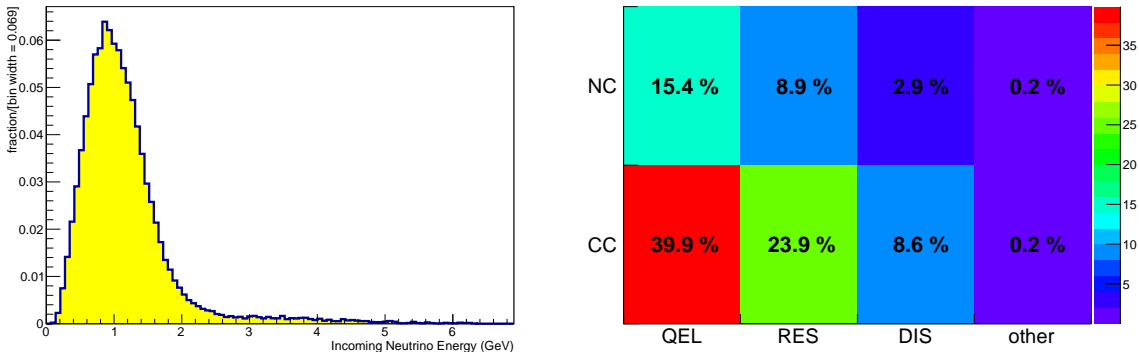


Figure 22: *Booster ν_μ interactions in iron as generated by GENIE. The distribution of incoming neutrino neutrino energy is shown in the left plot, while the rates of the single interaction processes are reported in the table at right.*

The propagation in the detector is implemented with either GEANT3.21 or FLUKA. The geometry of the detectors is described using FLUKA and ROOT geometry packages. The main features of the geometry implemented in the simulation are briefly described below. The spectrometer consists of 2 instrumented dipolar magnets. Each magnet is made of two magnetized iron walls producing a field of 1.5 T intensity in the tracking region; field lines are vertical and have opposite directions in the two adjacent walls whereas track bending occurs on the horizontal plane. The thickness of the iron planes is at

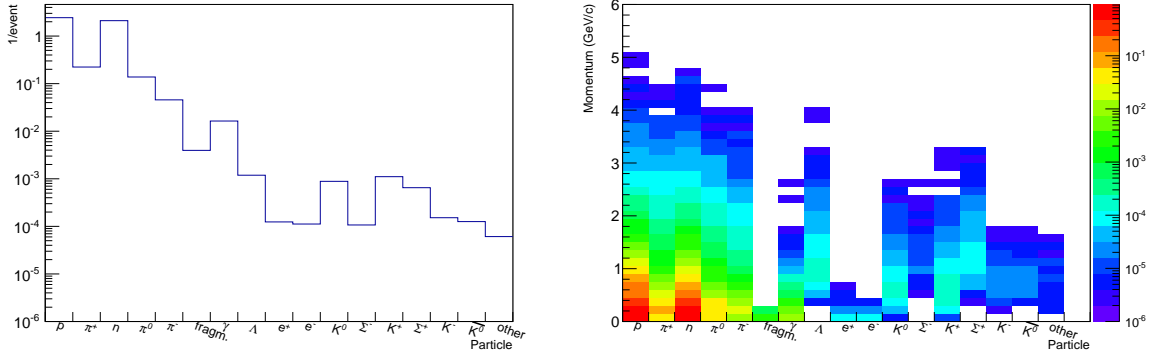


Figure 23: *Booster ν_μ interactions in iron: particles in hadronic system (left) and their momentum (right). These distribution are normalized to the total number of events.*

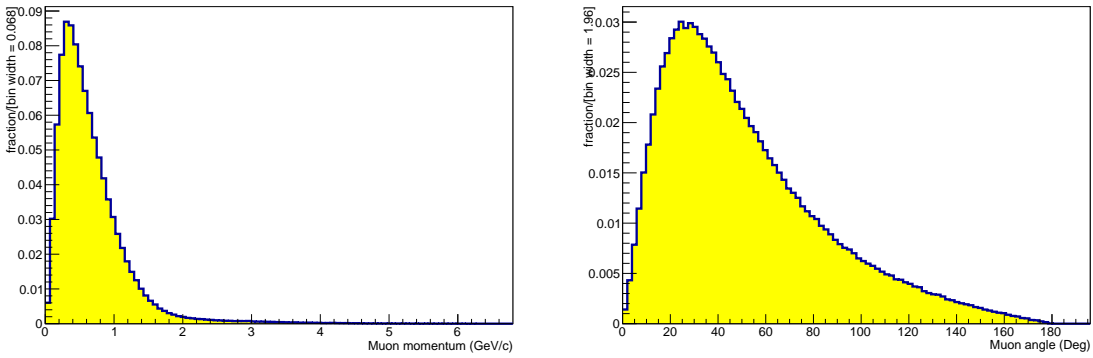


Figure 24: *Booster ν_μ CC interactions in iron: muon momentum (left) and angle (right).*

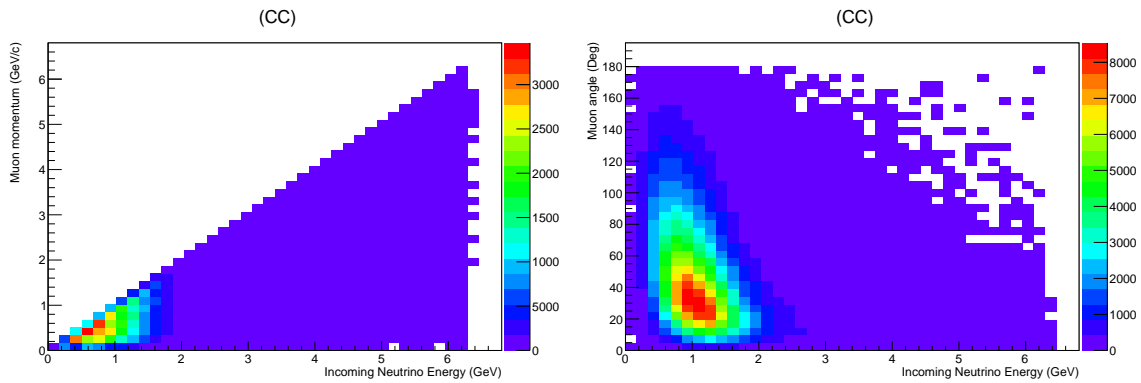


Figure 25: *Booster ν_μ CC interactions in iron: dependency of muon momentum (left) and angle (right) on the incoming neutrino energy.*

present envisaged to be 5 cm. Planes of bakelite RPC's are interleaved with the iron slabs of each wall to measure the range of stopping particles and to track penetrating muons. Each magnet is equipped with 22 planes of 4 rows, each consisting of 3 RPC's. The ND spectrometer is assumed to be similar to the FD (22 planes each with 3 rows and 2 columns of RPC's).

For the RPC's we assume digital read-out using 2.6 cm strip width and a position resolution of about 1 cm.

An event display of one booster neutrino ν_μ CC interaction in the spectrometer is shown in Fig. 26.

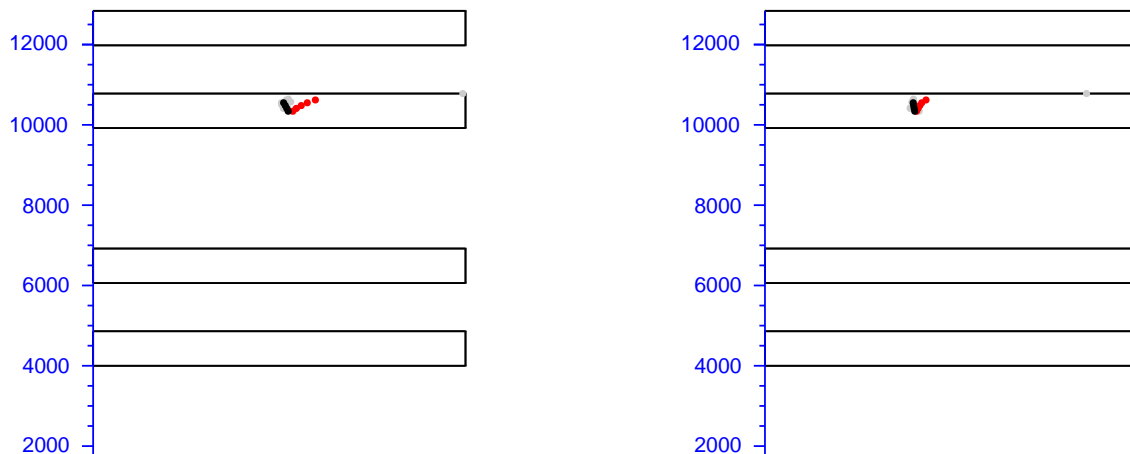


Figure 26: A event display of one Booster Neutrino CC Interaction in the spectrometer. The red dots are the hits of a muon track; the blacks of hadrons. The neutrino is coming from the bottom.

5.2 Reconstruction

A framework based on standard tools (ROOT, C++) has been developed for the reconstruction in both the Near and Far detectors. The reference frame is defined to have the Z -axis along the beam direction, Y perpendicular to the floor pointing upwards and X completing a right-handed frame. Event reconstruction is performed separately in the two projected views XZ (bending plane) and YZ (vertical plane).

A simple track model is adopted to describe the shape of the trajectory of tracks traveling through the detector. The model is based on the standard choice of parameters used in *forward* geometry (i.e. intercepts, slopes, particle momentum, particle charge etc.). The reconstruction strategy is optimized to follow a single long track (the muon escaping from the neutrino-interaction region) along the Z -axis.

The reconstruction is performed in the usual two steps: Pattern Recognition (Track finding) and Track Fitting. The task of the Pattern Recognition is to group hits into tracks. The Track Fitting has to compute the best possible estimate of the track parameters according to the track model. A parabolic

fit is performed in the XZ plane (bending) whereas a linear fit is used for YZ plane (vertical). Particle charge and momentum are determined from the track sagitta measured in the bending plane; the track fit is corrected for material interactions (Multiple Scattering and energy loss). Each spectrometer arm provides an independent measurement of charge/momentum. The implementation of a track fitting algorithm based on a *Kalman* filter is eventually foreseen.

A better estimation of the momentum is obtained by range for muons stopping inside the spectrometer.

Several observables are evaluated for each reconstructed event: i) number of fired RPC planes (NPLANES); ii) range in iron of the longest particle (RANGE). Their distribution are shown in Fig. 27.

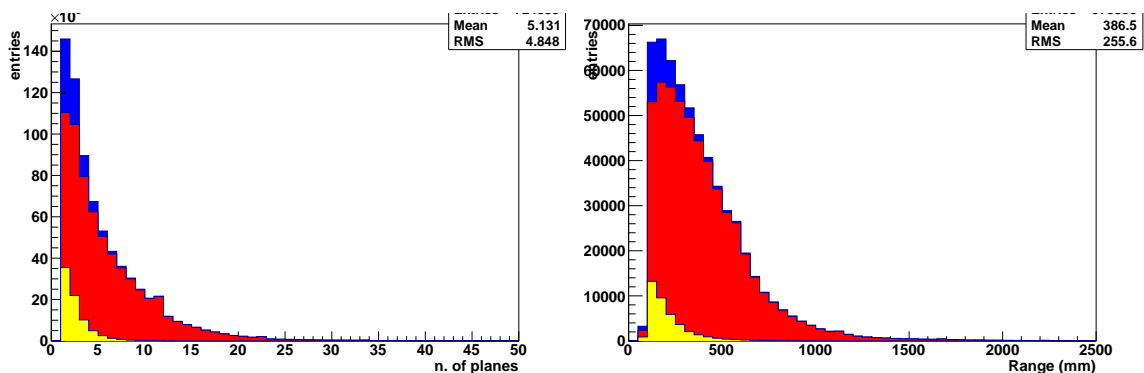


Figure 27: Distribution of Number of planes and Range for reconstructed events (FLUKA), for CC+NC (blue), CC (red) and NC (yellow)

The analysis is performed for three different samples: a) events which have at least 1 hit in the detector (CC+NC); b) charged current interactions (CC): c) quasi-elastic charged-current interactions (CCQE). For samples a) and b) we assumed perfect identification and background rejection capabilities. The dependency of reconstructed variables on muon momentum for sample CC and CCQE are shown respectively in Fig. 28 and Fig. 29.

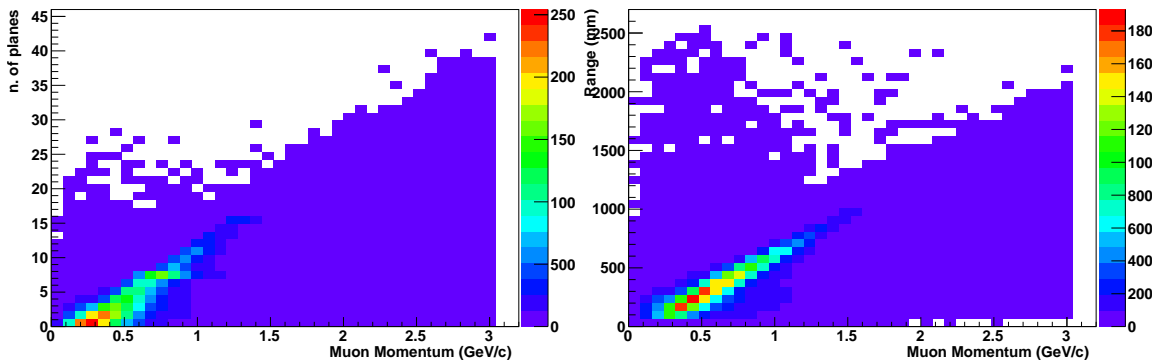


Figure 28: Number of planes and Range versus Muon Momentum (CC).

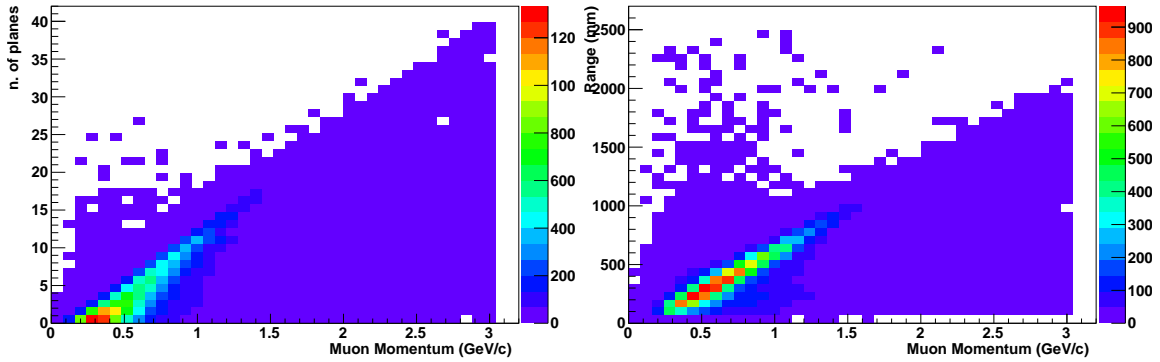


Figure 29: *Number of planes and Range versus Muon Momentum (CCQE).*

In order to evaluate the sensitivity of the experiment with the GLoBES tool, the response of the detector is expressed in terms of a function $R(E, E')$, i.e., a neutrino with a (true) energy E is reconstructed with an energy between E' and $E' + \delta E'$ with a probability $R(E, E')\delta E'$. The function $R(E, E')$ is also often called "energy resolution function"; its internal representation in the software is a smearing matrix.

In order to exploit the correlation between the number of planes (or range) and the neutrino energy in the charged current channel, we decided to describe directly the response of the detector in terms of a function $R(E, O)$, where O is one of such reconstructed variables. Smearing matrices and detector reconstruction efficiencies are shown in Fig. 30 and Fig. 31 (RANGE) as a function of NPLANES and RANGE, respectively, for several channels .

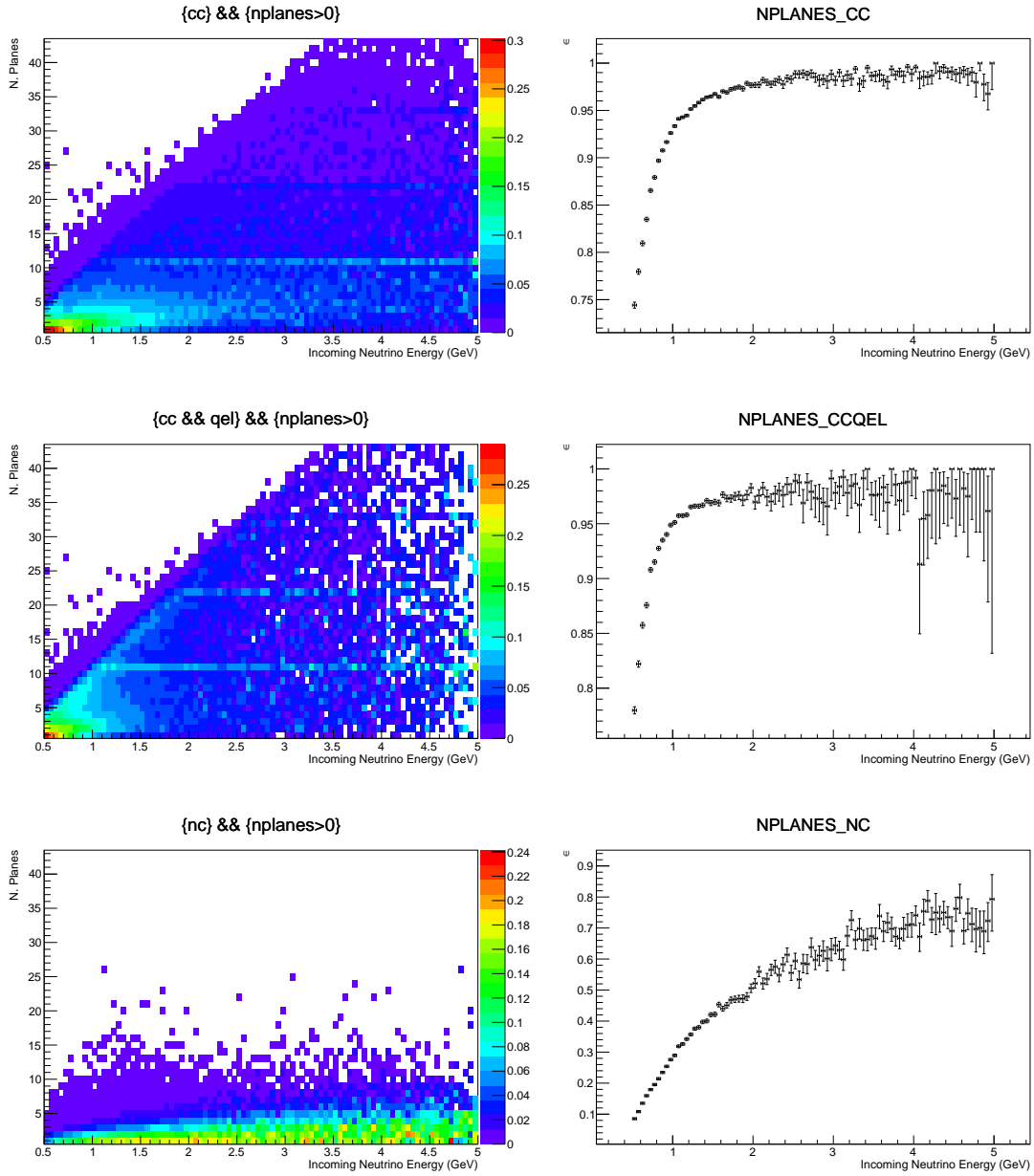


Figure 30: *Smearing matrix and efficiency for N Planes. In the top figures the whole CC sample is considered. The middle ones corresponds only to the CCQE sample, while the bottom ones corresponds to the NC channel.*

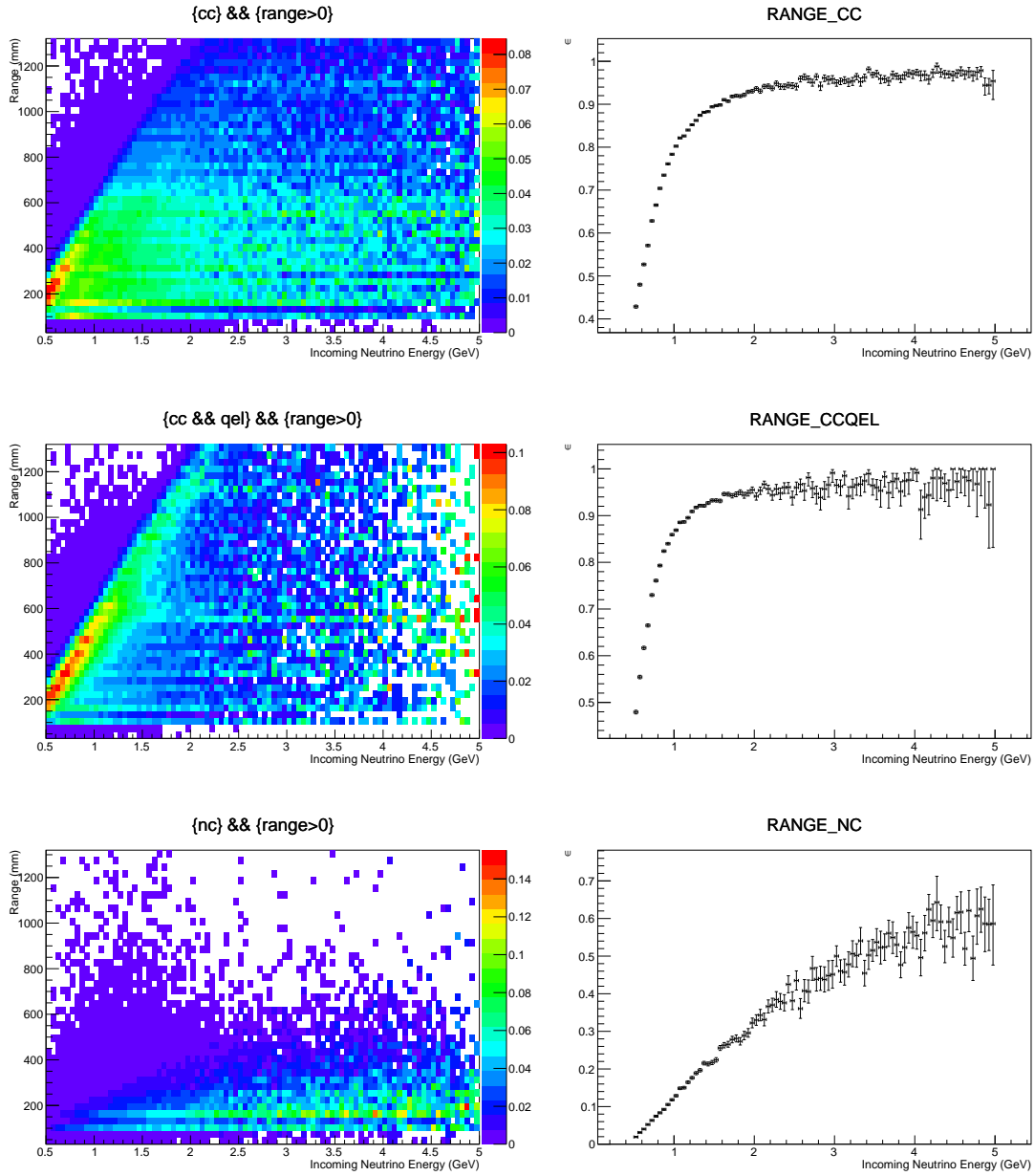


Figure 31: *Smearing matrix and efficiency for Range. In the top figures the whole CC sample is considered. The middle ones corresponds only to the CCQE sample, while the bottom ones corresponds to the NC channel.*

6 Mechanical Structure

The design of NESSiE spectrometers follows closely that of the OPERA apparatus, where iron dipole magnets are made of two vertical arms with rectangular cross-section and of top and bottom flux return yokes [23] (Fig. 32). Each arm is composed of 12 vertical layers of iron slabs, 5 cm thick, interleaved by 11 gaps 2 cm wide, hosting RPC detectors. Each iron layer, obtained by assembling 7 vertical iron slabs, covers a surface of $(8.75 \times 8.2) \text{ m}^2$. The magnet full height is about 10 m (including the top and bottom return yokes), its length along the beam is 2.85 m and its weight amounts to $\sim 1 \text{ kton}$. The slabs, the top and the bottom yokes are held together by means of screws, while more screws (about $1/\text{m}^2$) are used to keep slabs straight with spacers to ensure the thickness uniformity of the gaps hosting the detectors. The spectrometers are magnetized by coils located at the top and bottom return yokes, as shown in Fig. 32.

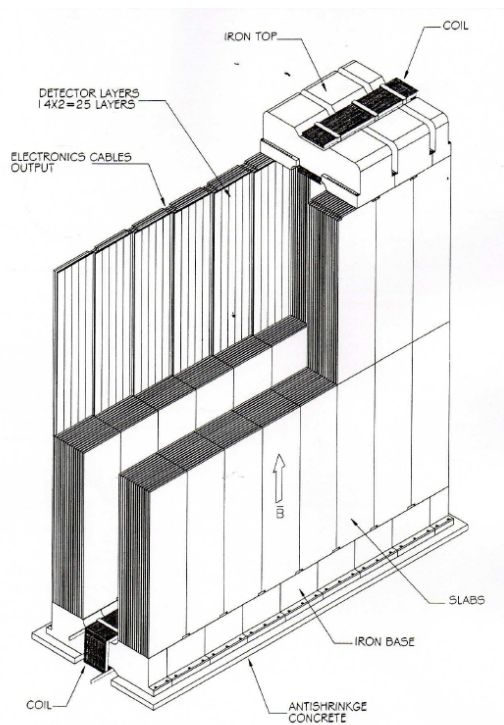


Figure 32: OPERA magnet scheme.

The installation of the OPERA magnets was performed according to the following time sequence:

- bottom yoke installation;
- internal support structure construction;
- iron/RPC layers installation (one plane in each arm at the time in order to keep the structure balanced);

- top yoke installation;
- removal of the internal structure.

For the NESSIE experiment a very similar setup should be used in order to profit of the available detectors, which were designed to provide the maximum acceptance coverage and strip signal configuration. The Far spectrometer is designed with the same width as in OPERA (i.e. 7 vertical iron slabs) but smaller height (4 rows of RPCs). The top and bottom return yokes are the same as the OPERA's ones. The two OPERA spectrometers will be coupled in the longitudinal view, by taking the 4/7 in acceptance for the Far site, while the remaining 3/7 will be used for the Near site. In the Near detector each iron wall, 3.4 m high, consists of 4 vertical slabs. The return yokes and the copper coils must be redesigned accordingly (Fig. 33). The size, mass and total instrumented surface of spectrometers are listed in Tab. 3.

Single-unit Spectrometer	Width (m)	Height (m)	Depth (m)	Total RPC Surface (m ²)	Total Iron Mass (ton)
Near	5.0	3.4	2.8	380	182
Far	8.8	4.5	2.8	880	423

Table 3: *Dimensions, instrumented surface and iron (slab) mass of the single-unit of the Near and Far spectrometers.*

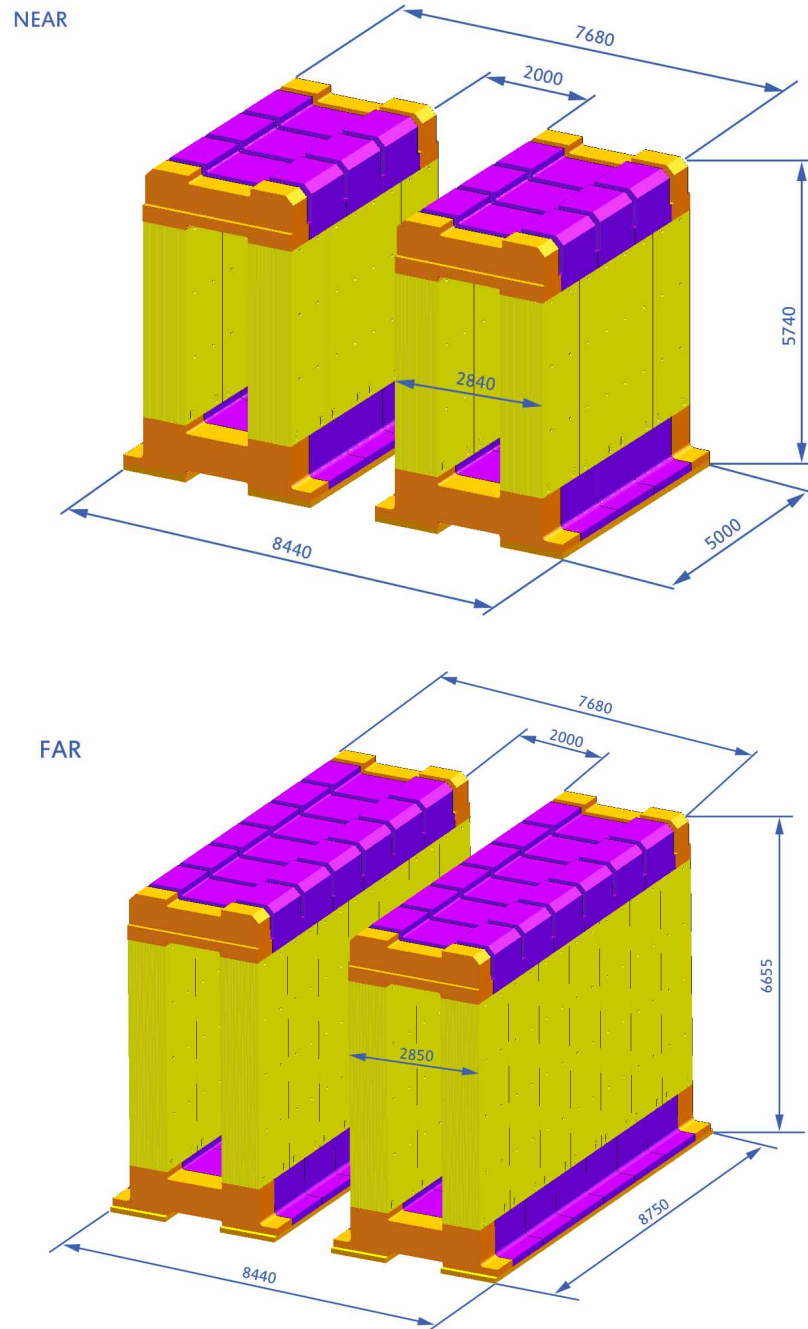


Figure 33: *NESSiE Near (top), Far (bottom) spectrometers*

7 Magnet Power Supply and Slow Control

The following description is based on the experience gained with the OPERA iron magnets (see [23] and references therein). We plan to adopt the same solution as for the OPERA spectrometers.

7.1 Power Supply features

The magnetomotive force to produce the magnetic field is provided by DC power supplies, located on the top of the magnet. They are single-quadrant AC→DC devices providing a maximum current of 1700 A and a maximum voltage of 20 V. As a single-quadrant power supply cannot change continuously the sign of the voltage, the sign of the current is reversed by ramping down the power supply and inverting the load polarity through a motorized breaker. The power supplies are connected to the driving coil wound in the return yokes of the magnet by means of short flexible cables.

Magnet Ancillary systems

- Coils: They are made of 100×20 mm² copper (type Cu-ETP UNI 5649-711) bars. The segments are connected through bolts after polishing and gold-plating of the contact surface. Each coil has 20 turns in the upper return yoke connected in series to 20 more turns in the bottom yoke. The two halves are linked by vertical bars running along the arm. Rexilon supports provide spacing and insulation of the bars.
- Magnet cooling system : Water heat exchangers are positioned between these supports and the bars while the vertical sections of the coil are surrounded by protective plates to avoid accidental contacts. More than 160 junctions were made for each coil and the quality of such contacts was tested measuring the overall coil resistance during mounting. The cooling system provides an operating temperature for the RPC detectors lower than 20 °C.

Status of the OPERA power supply units

- The overall downtime of the two OPERA magnets was about 0.1%. The power supply units of the first spectrometer stopped with a monthly frequency,^d while the 2nd power supply suffered no failures.

The NESSiE Far and Near magnets will be powered each by a power supply unit.

7.2 Monitored quantities for every magnet

The values to be monitored are:

^dNo firm conclusions about the cause of the failures was reached in 6 years of running.

- Continuous measurement of the magnetic field strength by Hall probes or pickup coils at magnet ramp down;
- electrical quantities:
 1. current: check for maximum/minimum range,
 2. voltage: check for maximum/minimum range,
 3. ground leakage current: check for maximum range (not automatically done in OPERA, via webcam or onsite check);
- temperatures and cooling:
 1. coil temperatures: check for maximum range,
 2. cooling water input temperature: check for maximum/minimum range,
 3. cooling water output temperature: check for maximum/minimum range,
 4. cooling water pressure, cooling water flux: check for maximum/minimum, values (not automatically done in OPERA, via webcam or onsite check).

7.3 The Slow Control System

The slow control system will monitor the whole hardware related Spectrometers, namely: the magnet power supplies, the active detectors and ancillary systems.

As it was done in the OPERA experiment [33] the NESSiE slow control system is organized in tasks and data structures developed to acquire in short time the status of the detector parameters which are important for a safe and optimal detector running.

The slow control should provide a set of tools which automatize specific detector operations (for instance the ramping up of the detector High Voltage before the start of a physics run) and let people on shift control the different components during data taking.

Finally, the slow control has to generate alarm messages in the event of a component failure and react promptly, without human intervention, to preserve the detector from possible damages. As an example the RPC High Voltage has to be ramped down at the occurrence of any gas system failure.

A possible structure of the slow control could be:

- a database is used to store both the slow control data and the detector configurations.
- the acquisition task is performed by a pool of clients, each serving a dedicated hardware component. The clients are distributed on various Linux machines and store the acquired data on the database.
- the hardware settings are stored in the database and served through a dynamic web server to all the clients as XML files. A configuration manager gives the possibility to view and modify the hardware settings through a Web interface.

- a supervisor process, the Alarm Manager, retrieves fresh data from the database, and is able to generate warnings or error messages in case of detector malfunctioning.
- the system is integrated by a Web Server for monitoring the global status of the data taking, the status of the various components, and to view the latest alarms.

8 Detectors for the Iron Magnets

The NESSiE Near and Far spectrometers will be instrumented with large area detectors for precision tracking of muon paths allowing high momentum resolution and charge identification capability. A spatial resolution of about 1 cm is enough.

Suitable active detectors for the ND and FD Iron spectrometers are RPCs – gas detectors widely used in high energy and astroparticle experiments [34] – because:

- they can cover large areas;
- they are relatively simple detectors in terms of construction, flexibility in operation and use;
- their cost is cheaper than other other large area tracking systems;
- they have excellent time resolution;
- and a high counting–rate power (in specific operational modes).

Furthermore by considering the remainders of the OPERA RPC production, about 1500 m² of RPCs are already available.

8.1 RPC Detectors

We plan to use standard bakelite RPCs: two electrodes made of 2 mm plastic laminate kept 2 mm apart by polycarbonate spacers, of 1 cm diameter, in a 10 cm lattice configuration. The electrodes have high volume resistivity (10^{11} – 10^{13} Ω ·cm). Double coordinate read–out is obtained by copper strip panels. The strip pitch can be between 2 and 3.5 cm in order to limit the overall number of read–out channels. An optimization of the strip size and orientation (horizontal, vertical and tilted ones) is required for the best track reconstruction resolution and reduction of ghost hits.

8.2 Detector Ancillary Systems

The operation of the RPCs requires:

- High Voltage system with current monitoring performed by dedicated nano–amperometers designed by the Electronics Service of INFN–LNF.

- monitoring of several environmental/operational parameters (RPC temperatures, gas pressure and relative humidity).
- Gas distribution system. Since the overall rate (either correlated or uncorrelated) is estimated to be low (see Sect. 9), standard gas mixtures for RPC in streamer operation can be used, like the one used in the OPERA RPCs, namely Ar/tetrafluorethane/isobutane and sulfur–hexafluoride in the volume ratios: 75.4/20/4/0.6.

The OPERA RPCs are flushed with an open flow system at 1500 l/h (5 refills/day). The installation of a recirculating system could also be considered if the gas flow has to be increased to prevent detector aging.

8.3 The Tracking Detectors for the Near and Far Spectrometers

The Near spectrometer will be a *calorimeter* made of planes of iron interlaced with planes of RPC, each of RPC unit being $2904 \times 1128 \text{ mm}^2$ in size. The RPCs will be arranged in planes of 2 columns and 3 rows, covering a surface of about 20 m^2 . A total of 44 planes (264 RPC units, 800 m^2 of detectors) will instrument the spectrometer.

The Far Detector will consist of 3 columns \times 4 rows of RPC to form planes of about 40 m^2 . As for the Near magnet 44 planes of detectors will be interleaved with iron absorbers amounting to 1760 m^2 (4528 units) of instrumented surface.

8.4 RPC Production and Quality Controls

As it was done for the OPERA experiment, before their installation, RPC will undergo a full chain of quality control tests, serialized according to the following steps:

- mechanical tests (gas tightness and spacer adhesion);
- electrical tests;
- efficiency measurement with cosmic rays and intrinsic noise determination.

The OPERA setup, in part still available at the Gran Sasso INFN Laboratories, was able to validate about 100 m^2 of RPCs per week.

8.5 Costs

The OPERA RPC are expected to be fully operative again. However, in case the percentage of breakages after dismantling were too high a new production could be foreseen^e. Plastic laminate can be produced in Italy by the Pulicelli company, located near Pavia (the company is currently producing material for the CMS RPC upgrade system). The cost of the plastic laminate is about 30

^eAbout 300 never used RPC detectors are also available from the OPERA contingency, i.e. about 1000 m^2 .

€/m². The RPC chamber assembly can be done in Italy by the renovated General Tecnica company at an estimated cost of about 300 €/m². The overall cost of an entire new RPC production is estimated of about 1.5 M€. The cost for 5000 m² of read-out strips is about 500 k€.

9 Backgrounds

The number of expected events from the Booster neutrino flux (Sect. 2) at the Near site is 0.1 event per spill (a spill being 1.6 μ s long within a cycle of 0.2 s). At the Far Detector the event rate is a factor of 20 smaller.

The background rate is estimated assuming a tracking system of single-gap RPC's. We distinguish the uncorrelated background due to detector noise and local radioactivity (dark counting rate) and the correlated background due to cosmic rays.

9.1 Uncorrelated Background

The dark counting rate depends on the detector features and ambient radioactivity. At sea level a typical rate for RPC is 300 Hz/m². Therefore the expected rate per plane is $\lambda_N = 300 \text{ Hz/m}^2 \times (5 \times 3.4 \text{ m}^2) \simeq 5.1 \text{ kHz}$ in the Near spectrometer and $\lambda_F = 300 \text{ Hz/m}^2 \times (8.7 \times 4.5 \text{ m}^2) \simeq 11.7 \text{ kHz}$ on the Far spectrometer.

With a time coincidence of at least three consecutive RPC planes within a time window of 300 ns the trigger rate per beam spill due to random coincidence is of the order of 3×10^{-6} and 4×10^{-5} for the Near and Far detector, respectively. This rate can be further suppress topological selection of the hits. Dark Noise events can be measured during the inter-spill time and subtraced statistically.

The number of fired strips depends on the strip width: with 2.6 and 3.5 cm strip-wide the typical cluster size is ~ 1.5 strips.

The requirement to be in the beam-spill time-window makes the dark noise contribution to the trigger rate negligible (see last column in Tab. 4).

9.2 Cosmic Ray Background

The contribution of Cosmic Ray (CR) muons to the plane-by-plane background is similar to the uncorrelated background, but long muon tracks can induce a more relevant background.

Assuming a trigger majority of ≥ 3 fired planes a cosmic ray muon can trigger the data-taking if it can cross at least 2 iron slabs ($2 \times 5 \text{ cm}$), namely if its momentum exceeds 250 MeV/c.

The integrated vertical muon flux is $J = 97 \text{ Hz/m}^2/\text{sr}$ at sea level [35]. The integrated vertical flux of the soft component (electrons and positrons), for $E \gtrsim 80 \text{ MeV}$, is $J(> E) = 0.22 E^{-1.45} [\text{Hz/m}^2/\text{sr}]$, where E is in GeV. Taking into account this contribution and minor ones due to hadrons, an integrated vertical CR flux at sea level of $J = 100 \text{ Hz/m}^2/\text{sr}$ will be used in the following

estimations. Under the conservative hypothesis of an isotropic CR ray flux equal to the vertical flux, the total rate λ_{RC} on a detector shaped as a fully efficient box is

$$\lambda_{RC} = \frac{\pi}{2} S_{tot} J$$

where S_{tot} is the detector surface. The expected number of CR events in a time window of $1.6 \mu s$ (the beam-spill time) is reported in Tab. 4. They scale with the time window T (by a factor $T/1.6 \mu s$). The data in Tab. 4 conservatively ignore that more detailed trigger conditions allow a significant reduction of the background.

Single Spectrometer	CR events in $1.6 \mu s$	Dark Noise events in $1.6 \mu s$	Beam events in $1.6 \mu s$
Near	4×10^{-2}	3×10^{-6}	10^{-1}
Far	7×10^{-2}	4×10^{-5}	5×10^{-3}

Table 4: Background events (CR muons and dark noise) and beam related events in the Near and Far spectrometers.

10 Read-out, Trigger and DAQ

10.1 DAQ overview

The aim of the DAQ is to read the signals produced by the electronic detectors and create a database of detected events. We recall in Tab. 5 the characteristics of the Booster primary proton beam. These are important inputs to define properly the data acquisition and flow.

The foreseen DAQ architecture is in three stages:

- the front-end electronics close to the detector (FEB)
- the read-out interface which together with the trigger board control the FEB read-out
- the Event Building which reconstructs events using standard workstations.

The whole event reconstruction is based on the time correlation of channels, which depends on the accuracy of the channel time stamping. A time resolution in the range $5 \div 10$ ns is sufficient to correctly associate the different hits to the corresponding events. A common time reference with respect to the Booster extraction time is used to time-stamp the data and to correlate the data of the various detectors.

Table 5: *Characteristics of the Booster primary proton beam*

	Booster Proton Beam
Proton beam momentum	8 GeV
Protons per pulse	4.5×10^{12}
Number of bunches	84
Bunch length	4 ns
Bunch spacing	19 ns
Burst length	1.6 μ s
Maximum repetition rate	0.2 s
Beam energy	5.8 kJ
Average beam power	30 kW

10.2 Data Flow

The Far detector is designed with 12 RPC/plane \times 11 planes/arm \times 2 arms \times 2 spectrometers for a total 528 RPC modules, 3 m² each. The Near detector is designed with 6 RPC/plane \times 20 planes/arm \times 2 arms \times 2 spectrometers for a total of 264 RPC modules.

Assuming a strip size of 2.6 cm along Y and 3.5 cm along X each Far detector plane will be equipped with $32 \times 4 = 128$ horizontal strips plus $112 \times 3 = 336$ vertical strips for a total number of about 500 electronic channels per plane. The total number of channels is therefore about 20,000. In the Near detector the number of electronic channels is about 290 per plane and the total number of channels is about 13,000.

The expected background rate due to the RPC single rate and the counts due to cosmic ray within the beam spill are reported in Sect. 9. With a maximum beam intensity of 4.5×10^{12} p.o.t. about 0.1 events are expected in the Near detector. Assuming four hit strips per plane and at most 16 byte of data per hit (channel address, signal and time) the size of the event after zero suppression is expected to be 1 kbyte.

10.3 Front-End- Electronics

The front-end electronics of the RPCs instrumenting the iron magnets was designed to operate with an event rate of the order of several tens of events per spill. A trigger-less logic has been implemented.

According to the same design scheme adopted for the OPERA experiment [36], groups of 64 signals coming from the RPCs working in streamer mode are read-out by means of front-end boards (FEB) equipped with 4 16-channel LVDS receivers and an Ethernet configurable Field Programmable Gate Array (FPGA), Fig. 34.

The LVDS receivers act as discriminators with programmable thresholds

that can be set via Ethernet by 4 integrated 10-bit DACs. The output of each discriminator is sampled with a resolution of 10 ns and continuously stored in a 4096-sample circular buffer whenever a write-enable signal is active. A time stamp with a 10 ns resolution is provided for each stored signal. Each FEB provides 2 FAST-OR signals implementing the trigger of groups of 32 channels.

FEBs are housed in crates controlled by a FPGA-based Crate Controller Board (CCB) with several tasks such as power supply management and monitoring, control signal distribution, masking, FAST-OR collection and management. Each CCB is able to manage up to 19 FEBs. The FAST-OR signals coming from the FEBs are stored in a circular buffer in a similar way as described above for the discriminated RPC signals in each FEB. The CCB provides 4 configurable FAST-OR signals as input to a Trigger Supervisor Board (TSB) able to generate a programmable trigger which can be used for the acquisition of cosmic ray muons as well as for monitoring and calibration purposes. Prototypes of FEBs and CCB are currently under test with RPC detectors exposed to cosmic rays .

The total estimated cost of the RPC read-out electronics is about 200 kEuro, taking into account 33000 digital channels.

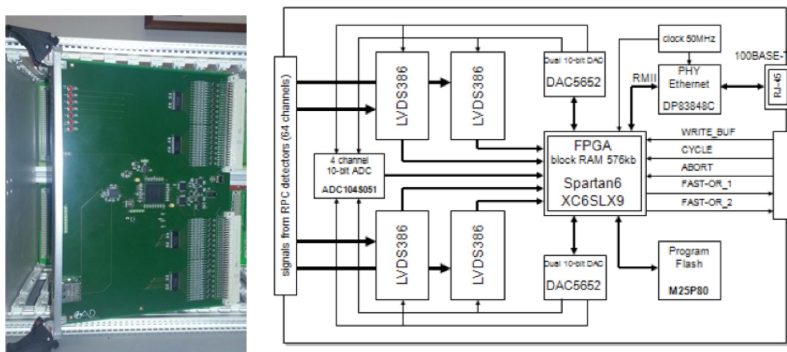


Figure 34: *The Front-End board for the RPC readout.*

10.4 DAQ

The Data Acquisition system is built like an Ethernet network whose nodes are the FEB equipped with an Ethernet controller. The Ethernet network is used to collect the data from the FEB, send them to the event building workstation and dispatch the commands to the FEBs for configuration, monitoring and slow control. This scheme implies the distribution of a global clock signal to synchronize the local counters running on the FEBs that are used to time stamp the data. The DAQ clock is synchronized with the FNAL accelerator timing system in order to start the DAQ readout cycle during particle extraction time.

Given the very short beam spill (1.6 μsec) the beam related events can be acquired in a trigger-less mode. Along the spill duration the FEBs store the status of the discriminators or the pulse height of the input signals, for digital

and analog readout, respectively, in a circular buffer driven by an on-board clock. The readout of the buffer by the DAQ is triggered by the *end-of-spill* signal sent to each FEB. This signal causes the FEB to disable the writing and time stamp information is generated concurrently on all FEBs. The time stamp is carried out on the trailing edge of the write signal, so the time information can be reconstructed backwards for all data. The duration of the write is also stored. The time-stamp information and the circular buffer content are then transferred through Ethernet to the event building^f.

In the inter-spill time the acquisition of cosmic ray muons and calibration data is triggered by a fake spill gate, possibly validated by a programmable logic (Trigger Board) on the basis of the FAST-OR- signals generated by the FEBs. The *start-of-spill* signal is used to abort all the readout process on the FEBs and to start new data read-out.

Assuming 64 channels per board, a clock of 10 ns and a buffer depth of 160, needed to acquire 1.6 μ sec of data, the time needed to transfer the data to the event building is about 100 μ sec on a Fast Ethernet.

The Event Builder should be based on standard commercial workstation. Data spying and monitoring process will also be implemented at this level.

11 FNAL Logistics, Schedule and Costs

The two experimental halls requested in the ICARUS proposal ([13]) to host the Near and Far detectors, are well suited for the two NESSiE spectrometers, too, even if, following our studies, a surface building is also suitable for our need. The main constraint is the need for a new pit in the Near site.

The Far detector experimental facility has to be placed 710 m from the production target. In principle this facility will may host two detectors and the related infrastructure: ICARUS T600 and NESSiE. NESSiE may be placed downstream the LAr TPC, minimizing the distance from ICARUS. In Fig. 35 the horizontal dimensions requested for the assembling of the spectrometers are outlined, while a 10×10 m² area would be finally used. Additional storage area is needed initially for the delivered detector parts and their pre-assembly. For the in-situ assembly of the NESSiE spectrometer a 25 ton crane capacity is required. The electrical power requirements are of the order of 100 KW for the NESSiE Far site. The experimental hall has to be equipped with a ventilation system in order to dissipate maximum 20 KW power and keep the room temperature below 27 °C due to the constraint of the running RPC.

The Near site spectrometer cross-section (5×5.35 m²) is about half the Far site spectrometer. The requested areas follow the same constraints of the Far site: they are reduced in X and Y while keeping the same length in Z . They are outlined in Fig. 36.

^fThe eventual correlation between spectrometer and LAr data can be achieved using a common clock signal to time-stamp the events. Data merging can therefore performed offline at the reconstruction level.

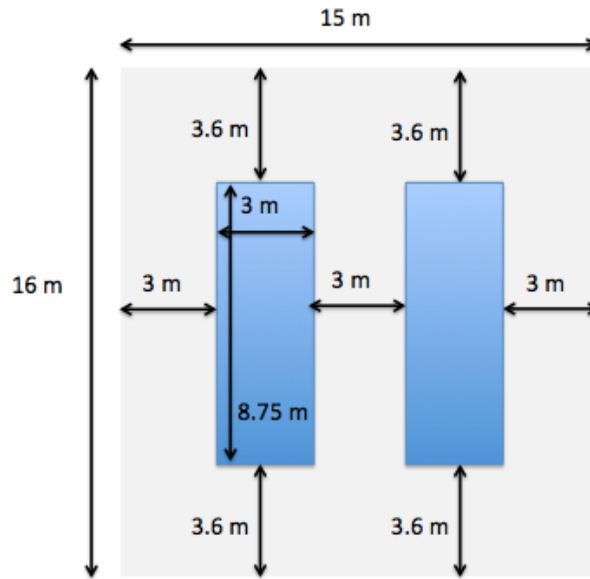


Figure 35: Description of the Far area needed for the in-situ assembling of the two spectrometer. The two 3.63 m lateral space are needed for the extraction of the internal support structure once the assembling is finished. The 3 m in the other direction are requested to ease the installation phase. Note that the minimum distance between the two magnets should be 2 m, as indicated in Fig. 33. Other $50 \div 100 \text{ m}^2$ are needed in a close site to keep the iron slabs and mechanical structures and to assemble RPCs during installation.

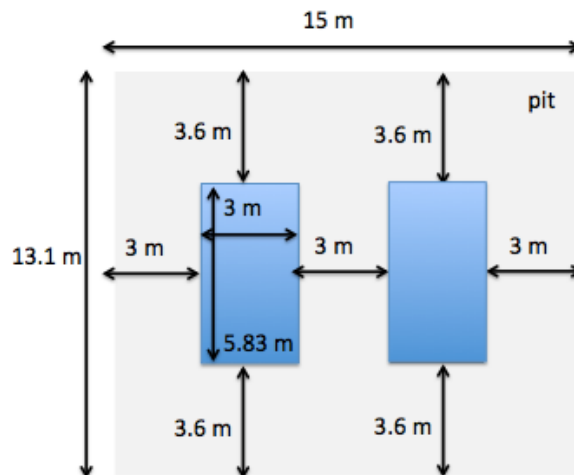


Figure 36: Description of the Near area needed for the in-situ assembling of the two spectrometer. The two 3.63 m lateral space are needed for the extraction of the internal support structure once the assembling is finished. The 3 m in the other direction are requested to ease the installation phase. Note that the minimum distance between the two magnets should be 2 m, as indicated in Fig. 33. The small space needed for the possible addition of a target is not included. Other $50 \div 100 \text{ m}^2$ are needed in a close site to keep the iron slabs and mechanical structures and to assemble RPCs during installation.

The spectrometers (the iron magnets and the RPC detectors), will be assembled in their final location, requiring sufficient surface area for the pre-assembly of components. The servicing systems are planned to be prepared mainly off line and eventually positioned, cabled and connected in the experimental hall.

11.1 Schedule and Costs

The choice of performing a design study that is *reliable* under several aspects led to make conservative, well controlled and realistic options. The re-use of systems developed for the OPERA experiment is envisaged. We note that the OPERA Spectrometers have been fully funded by INFN, except the Precision Trackers, which is therefore committed to their dismantling and entitled to possibly re-use them as well. In particular the choice to use detectors like the RPC ones and the development of dipole magnets which had, at least partly, already been constructed and have been in use, allows us to keep under control both the time schedule and the costs.

With respect to the schedule, which is reported in Tab. 6, it should be underlined that is based on the deep experience acquired with the OPERA Spectrometers, built up from 2005 to 2006 under critical conditions^g. The provisional areas and the experimental hall have to be ready for installation by the Fall 2016. The NESSiE installation will last conservatively 1.5 years, leaving six months commissioning period before the run start (assuming it is done almost simultaneously at the Near and Far sites, which is feasible with adequate manpower). The assumed exposure is 6.6×10^{20} proton-on-target (p.o.t.) to be delivered by the FNAL-Booster in 3 years of activity.

Year(portion)	Action
1 ^{rst} half 2015	Define tenders/contracts
2 nd half 2015	Site preparation Setting up Detectors Test-stands
1 ^{rst} half 2016	Mechanical Structure construction Start Magnet installation Start detectors installation
2 nd half 2016	End installation
1 ^{rst} half 2017	Commissioning and Starting Run
2 nd half 2019	End Data Taking

Table 6: *Tentative time schedule for the 2015–2019 years, including detector construction and installation at FNAL and data taking.*

With respect to the cost estimate, the expenses needed for the major items are reported in Tab. 7.

^gDuring the period 2005–2007 LNGS laboratory underwent restoration and safety works enforced by Italian Government, following the temporary seal of May 2005.

Item	Cost (in M€)
Far	
Magnet	2.5 (in-kind)
RPC detectors	0.8 (in-kind)
Strips	0.3 (in-kind)
New Electronics	0.2
Data Acquisition	0.1
Near	
Magnet	2.0 (in-kind)
Top/bottom yokes	1.0
Coils, Power Supplies	0.2
RPC detectors	0.6 (in-kind)
New detectors	0.2
Strips	0.2 (in-kind)
New Electronics	0.1
Data Acquisition	0.1
Transportation	0.6
Total	2.5 + 6.4 (in-kind)

Table 7: Estimate of the costs of the major items. Note the major costs for the Near site that include the duplicated parts of the OPERA spectrometers, i.e. the top and bottom closures, the coils and the power supplies. The cost for the possible construction of a small target with scintillators is indicated as "new detectors" in the Near set.

12 Physics Analysis and Performances

We developed sophisticated analysis to obtain the sensitivity region that can be achieved with an exposure of 6.6×10^{20} p.o.t., corresponding to 3 years of data collection at FNAL–Booster beam. Our guidelines have been the maximum extension at small values of the mixing angle parameter, as well as its dependence on systematic effects.

To this aim, three different analysis have been set up, of different complexity:

- the usual sensitivity plot based on the Feldman&Cousins technique (see Section V of [37]) has been obtained, by adding *ad hoc* systematic error evaluations;
- a full correlation matrix based on the full Monte Carlo simulation and reconstructed data;
- a new approach based on the profile CLs, similar to that used in the Higgs discovery.

Throughout the analysis the following framework has been considered. We assumed two identical muon spectrometers exposed to the Booster Neutrino Beam (BNB) located at a distance of 110 m (Near) and 710 m (Far) from the target and fiducial mass of 297 tons and 693 tons, respectively, as shown in Tab. 8.

	Fiducial Mass (ton)	Baseline (m)
Near	297	110
Far	693	710

Table 8: *Fiducial mass and baselines for Near and Far detectors.*

The number of expected events at Near and Far detector constitutes the primary input to compute the achievable sensitivity. The Booster Neutrino Beam (BNB) flux [38], as expected at 1 km from the source, is shown in Fig. 37, while the neutrino cross-sections for the different contributions of charged current (CC) and neutral current (NC) interaction (quasi-elastic, deep-inelastic-scattering and resonant) compared to the single quasi-elastic charged current (CCQE) interactions [27], as function of the incoming neutrino energy, are shown in Fig. 38. The convolution of flux and cross-sections implies the relevance of the CCQE component in our analysis that makes use of the muon momentum as estimator. To go from p_μ to E_ν either the usual formula in the CCQE approximation is applied

$$E_\nu = \frac{E_\mu - m_\mu^2/(2M)}{1 - (E_\mu - p_\mu \cos \theta)/M}, \quad (4)$$

(M being the nucleon mass) or it is extracted via Monte Carlo simulation.

For all the analysis the usual two-flavor neutrino mixing scheme is considered. The oscillation probability is therefore given by the formula:

$$P = \sin^2(2\theta_{new}) \sin^2(1.27 \Delta m_{new}^2 L(\text{km})/E(\text{GeV})) \quad (5)$$

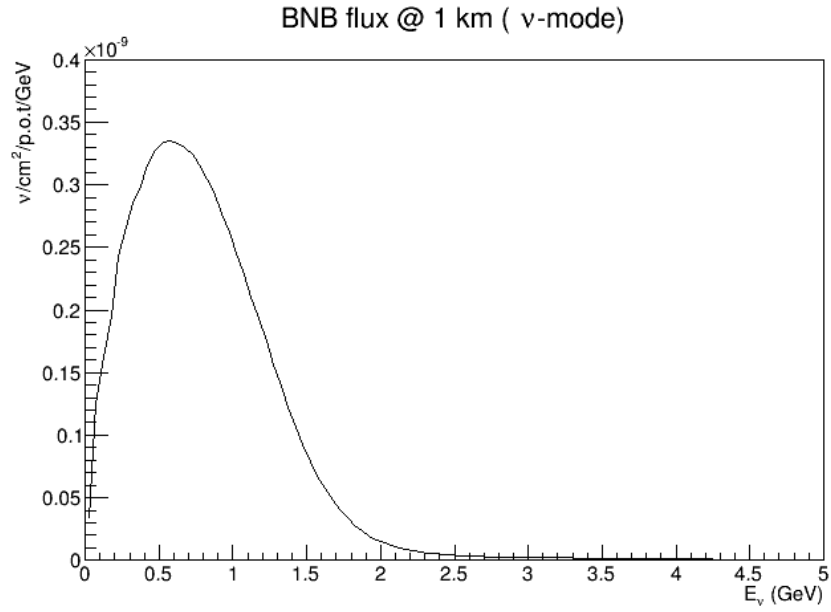


Figure 37: ν_μ BNB flux at a distance of 1 km from the neutrino source.

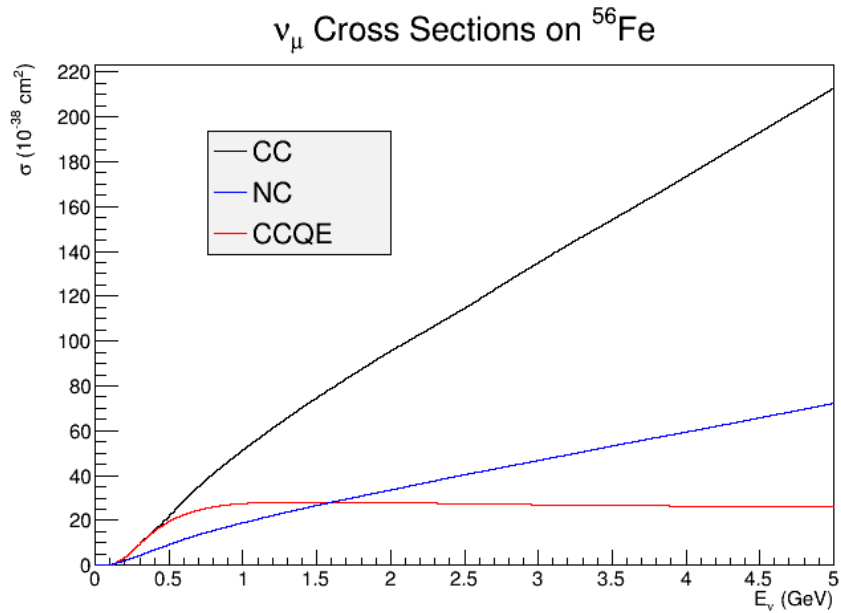


Figure 38: ν_μ cross-sections on ^{56}Fe for all (QE, Res, DIS) charged current (black) and neutral current (blue) interactions and for CCQE interaction (red), as extracted from GENIE [27].

where Δm_{new}^2 is the mass splitting between a heavy mass state and the heaviest of the three light neutrino mass states, and θ_{new} is the mixing angle between them. Then the disappearance of flavour α is due to the oscillation of neutrino mass states at the Δm^2 scale and at an effective mixing angle θ that can be simply parametrized as a function of the elements of a $3 + 1$ extended mixing matrix:

$$P(\nu_\alpha \rightarrow \nu_\alpha) = 1 - \sin^2(2\theta) \cdot \sin^2(1.267 \cdot \Delta m^2 \cdot L/E). \quad (6)$$

As L is fixed by the experiment location, the oscillation is naturally driven by the neutrino energy, with an *amplitude* determined by the mixing parameter.

The disappearance of muon neutrinos due to the presence of an additional sterile state depends only on terms of the extended PMNS [39] mixing matrix ($U_{\alpha i}$ with $\alpha = e, \mu, \tau$ and $i = 1, \dots, 4$) involving the ν_μ flavor state and the additional fourth mass eigenstate. In a $3+1$ model at Short Baseline (SBL) we have:

$$P(\nu_\mu \rightarrow \nu_\mu)_{SBL}^{3+1} = 1 - [4|U_{\mu 4}|^2(1 - |U_{\mu 4}|^2)] \cdot \sin^2 \frac{\Delta m_{41}^2 L}{4E}, \quad (7)$$

where $4|U_{\mu 4}|^2(1 - |U_{\mu 4}|^2)$ results as an *amplitude*.

In contrast, appearance channels (i.e. $\nu_\mu \rightarrow \nu_e$) are driven by terms that mix up the couplings between the initial and final flavour states and the sterile state yielding a more complex picture:

$$P(\nu_\mu \rightarrow \nu_e)_{SBL}^{3+1} = 4|U_{\mu 4}|^2|U_{e 4}|^2 \sin^2 \frac{\Delta m_{41}^2 L}{4E} \quad (8)$$

This also holds in extended $3 + n$ models.

It is interesting to notice that the appearance channel is suppressed by two more powers in $|U_{\alpha 4}|$. Furthermore, since ν_e or ν_μ appearance requires $|U_{e 4}| > 0$ and $|U_{\mu 4}| > 0$, it should be naturally accompanied by a corresponding ν_e and ν_μ disappearance. In this sense the disappearance searches are essential for providing severe constraints on the models of the theory (a more extensive discussion on this issue can be found e.g. in Sect. 2 of [40]).

It must also be noted that the number of ν_e neutrinos depends on the $\nu_e \rightarrow \nu_s$ disappearance and $\nu_\mu \rightarrow \nu_e$ appearance, and, naturally, from the intrinsic ν_e contamination in the beam. On the other hand, the amount of ν_μ neutrinos depends only on the $\nu_\mu \rightarrow \nu_s$ disappearance and $\nu_e \rightarrow \nu_\mu$ appearance but the latter is much smaller due to the fact that the ν_e contamination in ν_μ beams is usually at the percent level. Therefore in the ν_μ disappearance channel the oscillation probabilities in both Near and Far detectors can be measured without any interplay of different flavours, i.e. by the same probability amplitude.

The final distributions of events, either in the E_ν or the p_μ variables, normalized to the expected luminosity in 3 years of data taking at FNAL–Booster, or 6.6×10^{20} p.o.t., are reported in Fig. 39.

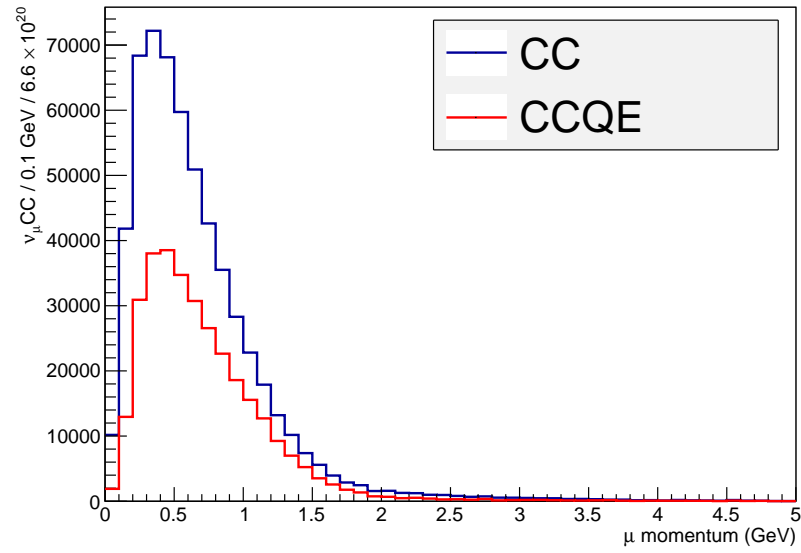
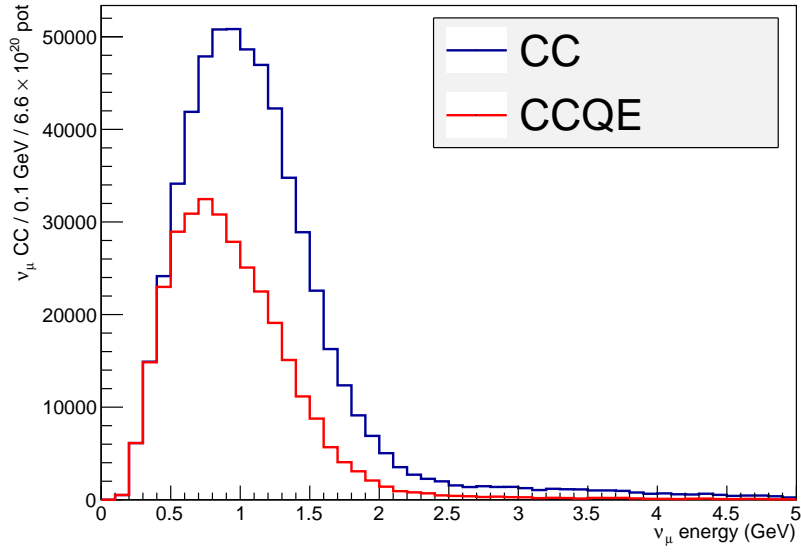


Figure 39: The absolute number of ν_μ CC interactions seen by the Far detector at 710 m, as a function of the E_ν (top) and the p_μ (bottom). The binning of 100 MeV has been that used further in all the statistical analysis.

12.1 Standard Sensitivity Analysis

A first basic estimate of the achievable performance has been obtained as follows:

1. spectra of p_μ at the Far and Near detectors (\vec{N}_0, \vec{F}_0) are generated in the null hypothesis (no disappearance signal) according to the expected event statistics. We use 50 bins from 0 to 5 GeV/c and only momenta above 0.5 GeV/c are considered.
2. We define the Far-to-Near ratio in each bin for these distributions as $R_{0,i} = F_{0,i}/(kN_{0,i})$ where k is a E_ν -independent factor to renormalizes Near and Far (i.e. without loss of generality for this study we neglect finite-distance effects).
3. For each $\sin^2(2\theta)$ and Δm^2 sampling point we calculate $R_i = N_i/(kF_i)$ obtained reweighing Monte Carlo interactions with a 2-flavour oscillation formula using the energy of the neutrino at true level.
4. A χ^2 is then defined for each $\sin^2(2\theta)$ and Δm^2 hypothesis as:

$$\chi^2 = \sum_{i=1}^N \left(\frac{1 - R_i/R_{0,i}}{\sigma_{R_{0,i}}} \right)^2 \quad (9)$$

where the error in each bin, $\sigma_{R_{0,i}}$, is simply the quadratic sum of the statistical term and a fixed (and bin-to-bin uncorrelated) systematic error $\sigma_{R_{0,i}} = R_{0,i} \sqrt{\frac{1}{N_{0i}} + \frac{1}{F_{0,i}}} \otimes \epsilon_{sys} R_{0,i}$. The sum is intended over the bins of the muon momentum distribution.

5. We find the point^h in the $(\sin^2(2\theta), \Delta m^2)$ plane giving the best description of the simulated data i.e. providing the minimum χ^2 : χ_{min}^2 .
6. We evaluate for each point in the $(\sin^2(2\theta), \Delta m^2)$ plane the difference $\Delta\chi^2 = \chi^2(\sin^2(2\theta), \Delta m^2) - \chi_{min}^2$
7. The 95% sensitivity region is then defined by selecting the portion of the parameter space for which the $\Delta\chi^2(\sin^2(2\theta), \Delta m^2)$ is larger than 5.9915 (assuming a 2-DOF χ^2 distribution for $\Delta\chi^2$).

Results are shown in Fig. 40 for a set of ten simulated null experiments. The top plot assumes $\epsilon_{sys} = 0$ while the bottom plots assumes $\epsilon_{sys} = 0.01$.

In the Feldman&Cousins approach a cut depending on $\sin^2(2\theta)$ and Δm^2 is applied in place of a fixed value (5.9915): $\Delta\chi_{cut}^2(\sin^2(2\theta), \Delta m^2)$. The critical value has been determined as follows: for every $\sin^2(2\theta), \Delta m^2$ sampling point, oscillated spectra have been generated and fitted thus defining a χ_{min}^2 . The distribution of $\Delta\chi^2(\sin^2(2\theta), \Delta m^2)$ is taken and $\Delta\chi_{cut}^2(\sin^2(2\theta), \Delta m^2)$ is the value for which obtaining a larger $\Delta\chi^2$ has only a 5% probability. We have verified that the limits obtained with a variable critical value for the χ^2 provide limits which are very close to the ones obtained using a fixed cut.

^hUsing the gMINUIT ROOT package.

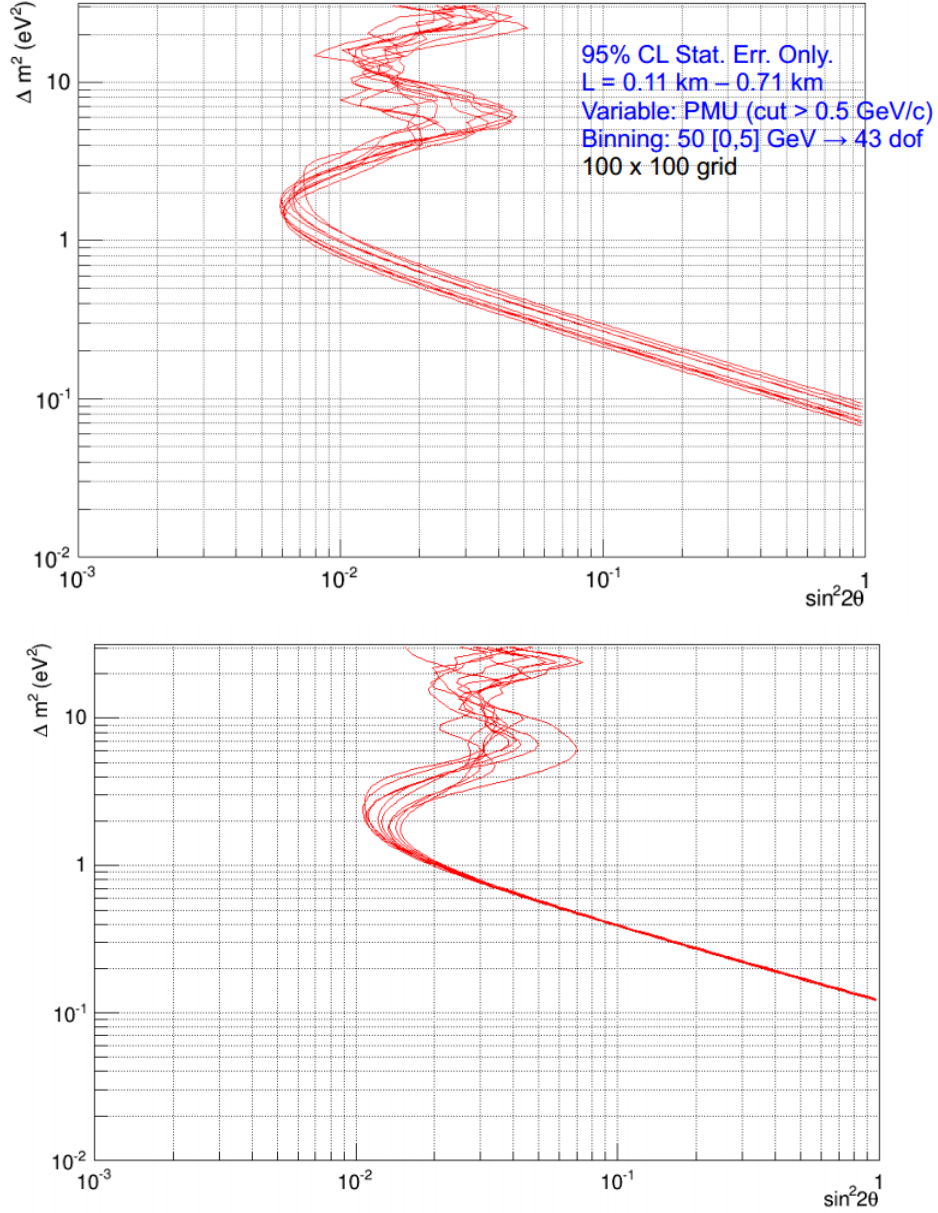


Figure 40: *Top. Sensitivity curves at 95% C.L. with ten simulated toy experiments assuming full statistics and no systematic uncertainties. p_μ is used as observable above 500 MeV/c in the fit. Baselines are set at 110 and 710 m. We use total of 10^4 sampling points uniformly distributed in log scale. Bottom. As above but using $\epsilon_{sys} = 0.01$.*

12.2 Full simulation and Matrix–Correlation

In this analysis we implemented different smearing matrices for two different observables, the muon *range* and the *number of crossed planes*, associated with the true incoming neutrino energy. These matrices were obtained through the Monte Carlo simulation described in Sect. 5 and reported here for convenience. In Fig. 41 are shown the smearing matrices for the observable number of planes for CC, CCQE and NC events, while in Fig. 42 are plotted the smearing matrices for the range estimator for CC, CCQE and NC events.

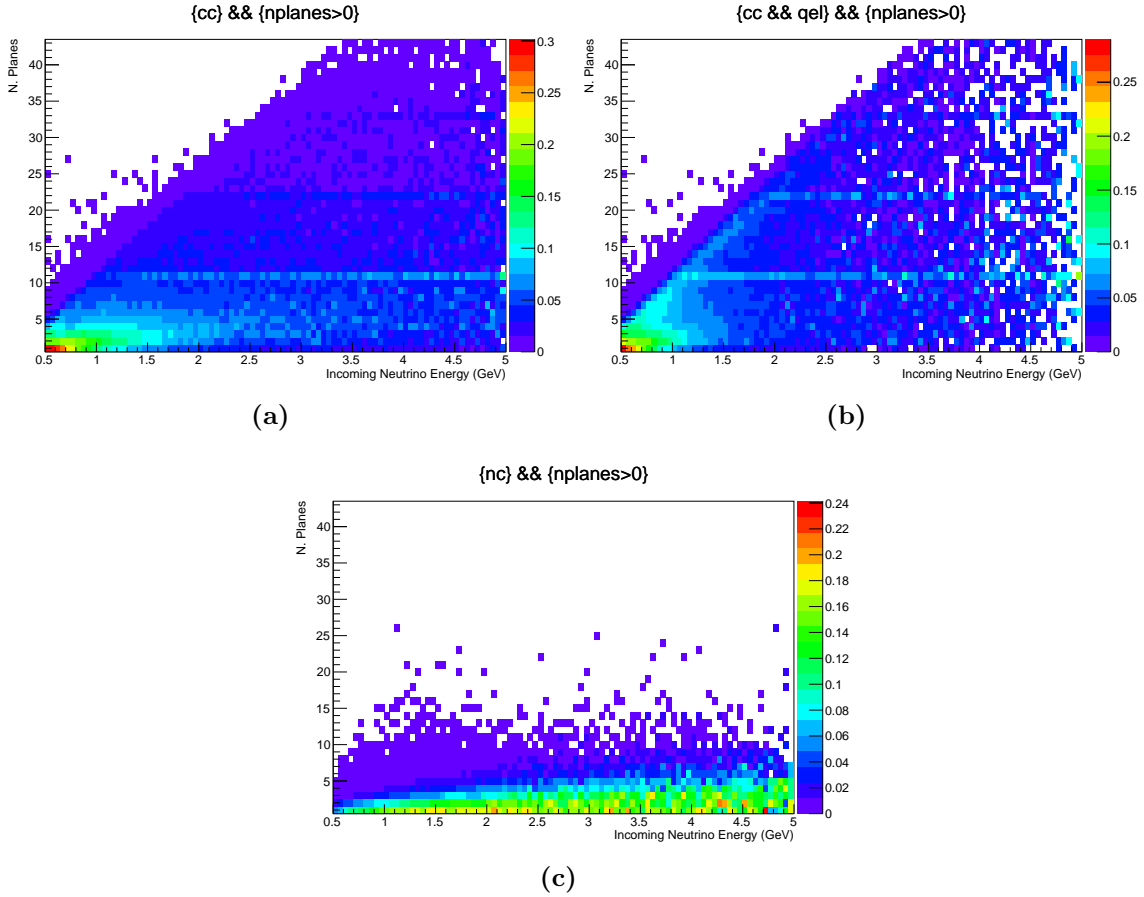


Figure 41: Smearing matrix of the reconstructed number of planes for CC (a), NC (b) and CCQE (c) events without cut on the number of planes.

12.2.1 Observables spectrum evaluation

We studied the sensitivity to the ν_μ disappearance using two different observables: the range and the number of planes as shown in the previous section. We divide range spectrum in 43 uniform bins between 30 and 1320 mm, number of planes spectrum in 43 bins between 1 and 43, while for neutrino energy spectrum we choose a 90 equidistant sampling from 0.5 to 5 GeV/c.

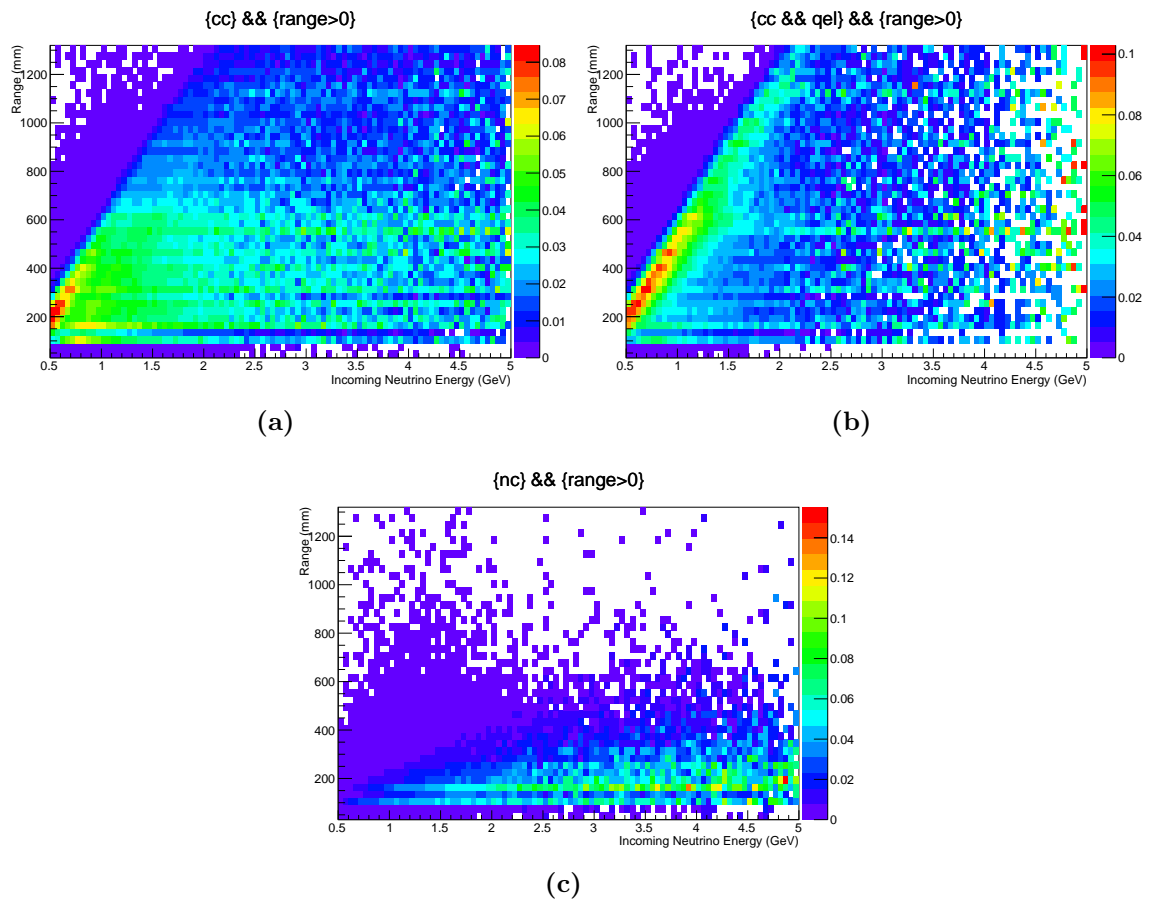


Figure 42: Smearing matrix of the reconstructed range for CC (a), NC (b) and CCQE (c) events without cut on the range.

The range and the number of planes spectrum at Near and Far detector were evaluated using GLOBES [41]. If we denote with E_i^{Far} and E_i^{Near} the number of expected events in i -th bin for the Far and Near detector, respectively, then we can define N_i^{Far} and B_i^{Far} as:

$$N_i^{Far} = E_i^{Far} \quad (10)$$

$$B_i^{Far} = E_i^{Near} \left(\frac{m_{Far}}{m_{Near}} \right) \left(\frac{L_{Near}}{L_{Far}} \right)^2 \quad (11)$$

where m_{Far} and m_{Near} denote the mass of Far and Near detector, respectively, and L_{Near} and L_{Far} are the distances for the Near and Far detector from the neutrino source. B_i^{Far} represents the number of expected events at Far detector by scaling the number of expected events at the Near detector for the ratio of the masses and the squared ratio of their baseline. B_i^{Far} is the number of expected events at Far site without oscillations, while N_i^{Far} is the number of expected events at Far detector which depends on the oscillation probability.

12.2.2 Results

To determine the exclusion region in the oscillation parameter plane $\Delta m_{new}^2 - \sin^2(2\theta_{new})$ we evaluate B_i^{Far} and N_i^{Far} for each value of Δm_{new}^2 and $\sin^2(2\theta_{new})$ and we calculate the χ^2 :

$$\chi^2 = \sum_{i=0}^{N-1} \sum_{j=0}^{N-1} (B_i^{Far} - N_i^{Far})(M^{-1})_{ij}(B_j^{Far} - N_j^{Far}) \quad (12)$$

where N is the number of bins and M is the covariance matrix [42] which take into account the uncertainties and their bin-to-bin correlations [43]. The covariance matrix is constructed as:

$$M = M^{stat} + M^{norm} + M^{shape} \quad (13)$$

where M^{stat} is the statistical errors matrix, M^{norm} is the normalization errors matrix and M^{shape} is the shape errors matrix. Statistical errors are added to the diagonals terms of the covariance matrix and are evaluated as:

$$M_{ij}^{stat} = B_i^{Far} \delta_{ij} \quad (14)$$

It is possible to observe ν_μ disappearance either from a deficit of events (normalization) or, alternatively, from a distortion of the observable spectrum (shape) which are affected by systematic uncertainties expressed by the normalization errors matrix and the shape errors matrix. The normalization errors matrix is the component of error matrix which is the same for each element. This term is associated with the normalization uncertainty applied to each bin as:

$$M_{ij}^{norm} = \epsilon_{norm}^2 B_i^{Far} B_j^{Far} \quad (15)$$

where ϵ_{norm} is the normalization error. The shape errors matrix represents a migration of events across the bins. In this case the uncertainties are associated with changes where the total number of event remains unchanged and so a depletion of events in the some region of the spectrum should be compensated by an enhancement in others. In our model we choose a shape error matrix that satisfies the following constrains:

$$(N_i^{Far} - B_i^{Far}) \propto i \quad (16)$$

$$\sum_{i=0}^{N-1} (N_i^{Far} - B_i^{Far}) = 0 \quad (17)$$

$$\sum_{i=0}^{N/2} (N_i^{Far} - B_i^{Far}) = I\epsilon_{shape} \quad (18)$$

In this case the shape errors matrix elements are:

$$M_{ij}^{shape} = \left[\left(\frac{N-1}{2} \right) - i \right] \left[\left(\frac{N-1}{2} \right) - j \right] \left(\frac{8\epsilon_{shape}I}{N^2} \right)^2 \quad (19)$$

where $I = \sum_{i=1}^N B_i^{Far}$ and ϵ_{shape} is the shape error. We use frequentist methods to study the χ^2 statistic distribution in order to calculate the sensitivity for oscillation parameters. In Fig. 43 (top) are shown sensitivity plots obtained using the range as observable without cuts, while in Fig. 43 (bottom) are presented sensitivity plots obtained using the number of planes without cuts on the observable. From these plots it can be seen that sensitivity computed considering CC and NC events is almost the same as the sensitivity obtained with only CC events and therefore NC background events don't affect the sensitivity.

We studied the sensitivity with different cuts on the range (Fig. 44 (top)) and on the number of planes (Fig. 44 (bottom)). Then we calculated sensitivity plot introducing bin-to-bin correlated systematic uncertainties as expressed in the covariance matrix in Eq. 13. In Fig. 45 is shown the sensitivity calculated considering 1% correlated error in the normalization, while in Fig. 47 is plotted the sensitivity calculated considering 1% correlated error in the shape. It is interesting to outline that the level of the systematic normalization error affects the sensitivity region only at the extreme edges at small values of the mixing parameter. This is demonstrated in Fig. 46.

The sensitivity plots calculated without correlated errors but with uncorrelated bin-to-bin uncertainties (1%) are shown in Fig. 48 for both the observables. In Fig. 49 we present also sensitivity plot obtained with 2% uncorrelated error, which in our analysis represents the upper limit for the sensitivity.

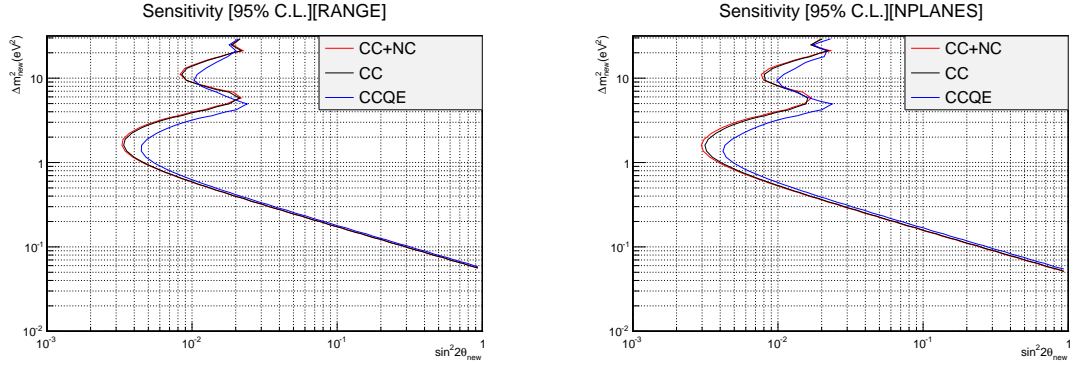


Figure 43: 95% CL sensitivity obtained using range (top) and number of planes (bottom) for all (QE, Res, DIS) CC (black) and CC+NC (red) events and for only CCQE events (blue). In this case we considered no systematic errors and no cuts on the observables.

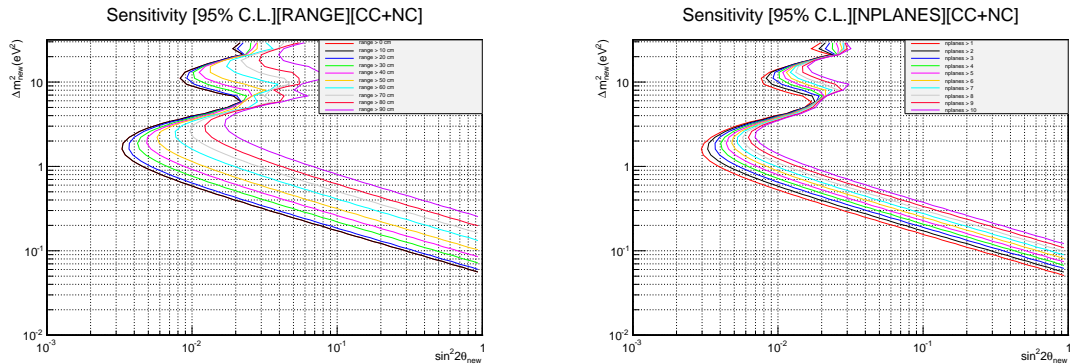


Figure 44: 95% CL sensitivity for different range cuts (top) and for different cuts in the number of planes (bottom) for CC+NC events. The sensitivity was obtained considering no systematic errors.

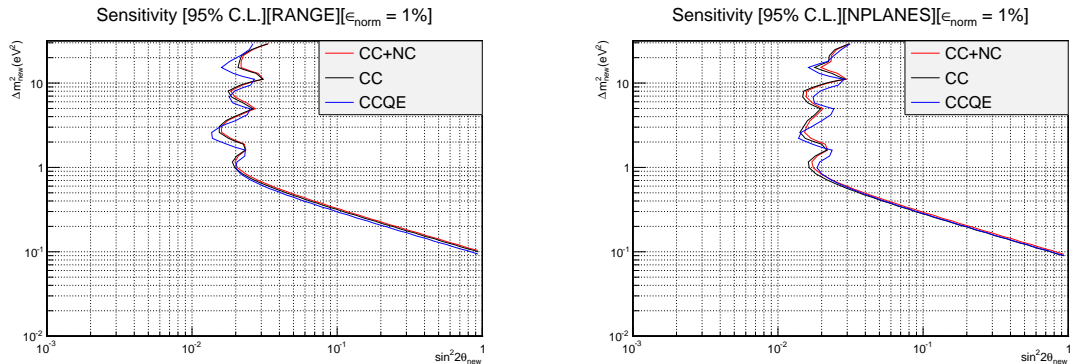


Figure 45: 95% CL sensitivity obtained using range (top) and number of planes (bottom) for all (QE, Res, DIS) CC (black) and CC+NC (red) events and for only CCQE events (blue). In this case we considered 1% bin-to-bin correlated error in the normalization.

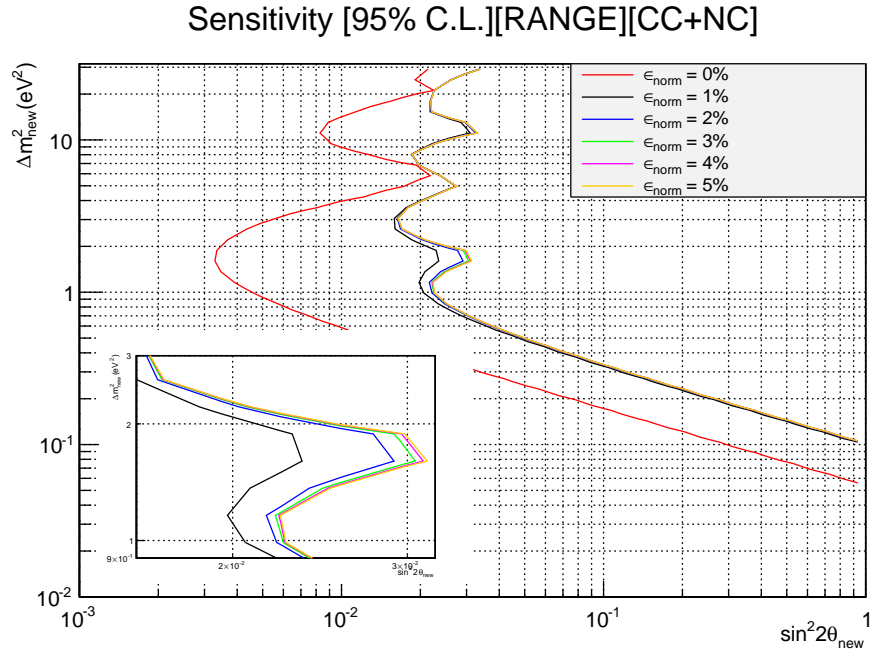


Figure 46: With the same condition of the previous figure (Fig. 45: 95% CL sensitivity obtained using range (top) and number of planes (bottom) for all CC+NC events) the systematic bin-to-bin correlated error on the normalization has been increased up to 5%. The 5% curve actually stays below the 4% one. In the insets a zoom of the region around 1 eV² and 0.02 in sin²(2θ) is given.

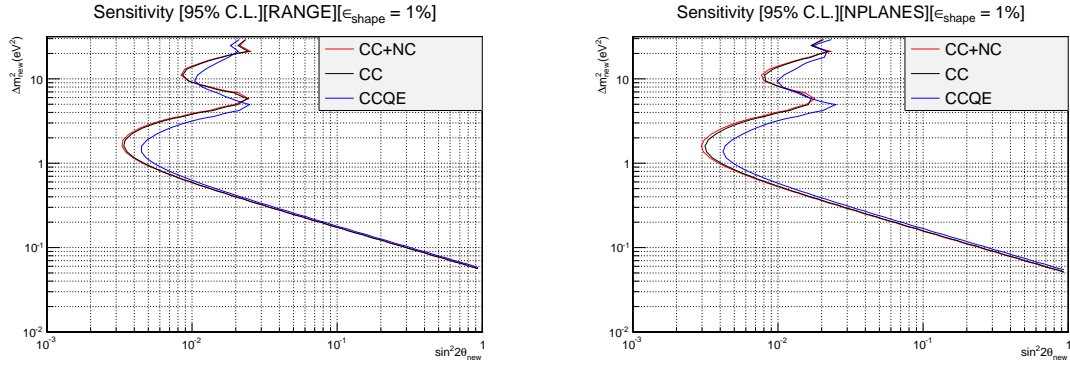


Figure 47: 95% CL sensitivity obtained using range (top) and number of planes (bottom) for all (QE, Res, DIS) CC (black) and CC+NC (red) events and for only CCQE events (blue). In this case we considered 1% bin-to-bin correlated error in the shape.

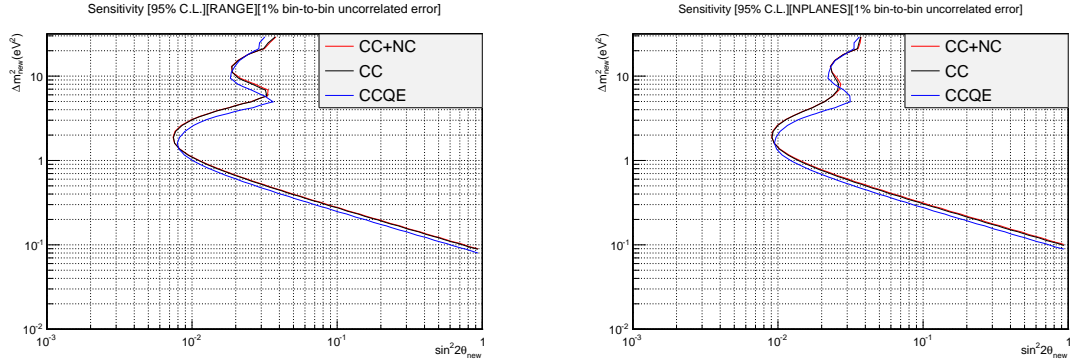


Figure 48: 95% CL sensitivity obtained using range (top) and number of planes (bottom) for all (QE, Res, DIS) CC (black) and CC+NC (red) events and for only CCQE events (blue). In this case we considered only a bin-to-bin uncorrelated error of 1%.

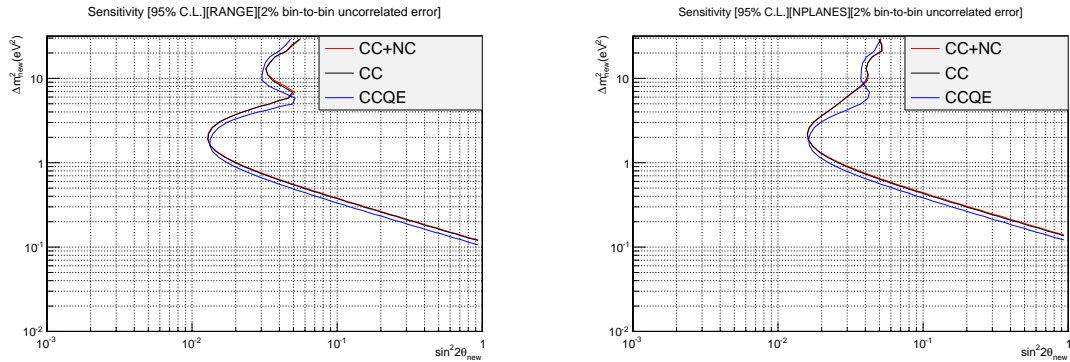


Figure 49: 95% CL sensitivity obtained using range (top) and number of planes (bottom) for all (QE, Res, DIS) CC (black) and CC+NC (red) events and for only CCQE events (blue). In this case we considered only a bin-to-bin uncorrelated error of 2%.

12.3 Profile CLs

In this method we introduce a new test-statistics that depends on a *signal-strength* variable. We may observe that, by looking at Eq. 5, for a fixed Δm_{new}^2 , the first factor, $\sin^2(2\theta_{new})$, acts as an amplification quantity of the configuration shape of the estimator in using. Then, we may identify the signal-strength μ with $\sin^2(2\theta_{new})$ and construct the estimator function:

$$f = \frac{1 - \mu \cdot \sin^2(1.27 \Delta m_{new}^2 L_{Far}/E)}{1 - \mu \cdot \sin^2(1.27 \Delta m_{new}^2 L_{Near}/E)} \quad (20)$$

Whether, for example, the *benchmark* values $\Delta m_{new}^2 = 1 \text{ eV}^2$ and $\sin^2(2\theta_{new}) = 0.03$ are considered, once the Far and Near distributions have been properly normalized, the observed oscillation shapes are depicted in Fig. 50.

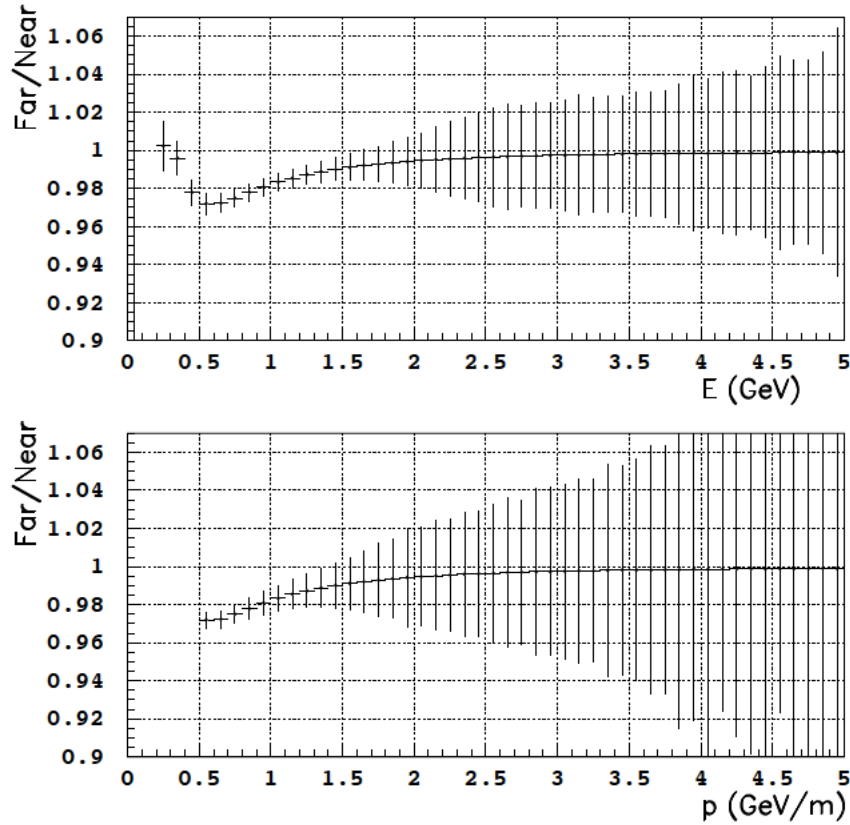


Figure 50: The observable oscillation patterns as function of E_ν (top) and p_μ (bottom) for the best fit point of [44], $\Delta m^2 = 1 \text{ eV}^2$ and $\sin^2(2\theta) = 0.03$. The error bars correspond to the full statistical error given by 3 years of data taking at the FNAL-Booster, or $6.6 \times 10^{20} \text{ p.o.t.}$ A cut of 500 MeV has been applied on the muon momentum in the bottom plot.

From the pattern of Fig. 50 two different likelihood functions can be constructed, one for the *background-only* hypothesis and one for *signal + back-*

ground:

$$L_{bck}(data|0) = \prod_{bins} G(data|\alpha_i, \sigma_i)$$

$$L_{sign+bck}(data|\mu) = \prod_{bins} G(data|\alpha_i \otimes \mu, \sigma_i)$$

where G is just the Poisson (or the Gaussian, in our case, provided the large number of events collected) distribution centered in α_i with dispersion σ_i , and μ is the *strength*. The usual estimator q can be further elaborated:

$$q_0 = -2 \ln \frac{L(data|0)}{L(data|\mu)}$$

If one allows μ to be as large as possible to be observed at e.g. at a 95% C.L., then two p -values can be computed for the *background-only* and the *signal + background* hypothesis. The test statistics becomes:

$$CL_S = \frac{p_{val}(\mu \cdot signal + background)}{1 - p_{val}(background)}$$

Finally, μ has to be adjusted until $CL_S = 0.05$ is reached. Note that in our case the possibility to use the Gaussian distribution brings to a simple expression for q_0 :

$$\begin{aligned} q_0 &= -2 \ln L(data|0) + 2 \ln L(data|\mu_{best}) \\ &= -2 \sum \left(\ln \frac{1}{\sqrt{\pi}} + \ln \frac{1}{\sigma} - \frac{x-1}{2\sigma^2} \right) \\ &\quad + 2 \sum \left(\ln \frac{1}{\sqrt{\pi}} + \ln \frac{1}{\sigma} - \frac{x-\mu_{best}}{2\sigma^2} \right) \\ &= \sum \frac{1}{\sigma^2} \left((x-1)^2 - (x-\mu_{best})^2 \right) \\ &= \chi_0^2 - \chi_{best}^2 \end{aligned}$$

where for each bin it holds $\sigma = \left(\frac{N_{Far}}{N_{Near}} \cdot Rate \right) \sqrt{\frac{1}{N_{Far}} + \frac{1}{N_{Near}}}$ with obvious meaning for the symbols, while μ_{best} is obtained by fitting over Eq. 20. Note that this procedure is named *raster-scan* by [37] even if no CL_S estimator is considered there.

In a simplified way, for each Δm^2 a sensitivity limit can be obtained from the p -value of the distribution of the estimator in Eq. 20, in the assumption of *background-only* hypothesis. The corresponding sensitivity is shown in Fig. 51.

That procedure does not correspond to compute the exclusion region of a signal, even if it provides confidence for it. The exclusion plot should be obtained by fully developing the CL_S procedure as outlined above. However, since we are first interested in exploiting the sensitivity of our experiment to any oscillation pattern not compatible with the standard 3-neutrino scenario,

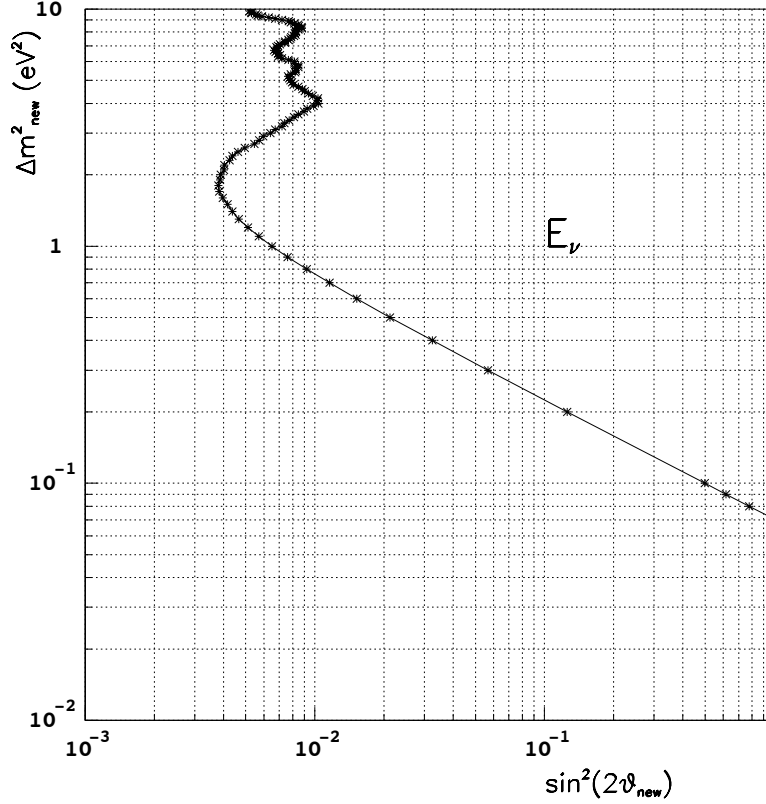


Figure 51: The sensitivity plot obtained by computing the modified raster-scan method, in a CL_S framework. The energy of the neutrino has been evaluated via Monte Carlo in the hypothesis of CCQE events. A conservative cut of $p_\mu \geq 500$ MeV has been applied.

the above procedure provides insights to such question, and it is fully compatible with the previous two analysis and the usual neutrino analysis found in literature.

Moreover, following the same attitude, an even more *aggressive* procedure can be applied. Since the deconvolution from p_μ to E_ν introduces obviously a degeneration of the information, we may want to check whether the more direct and measurable estimator, p_μ , is a valuable one. In such a case Eq. 20 becomes:

$$f = \frac{1 - \mu \cdot \sin^2(1.27 \Delta m^2 L_{Far}/p_\mu)}{1 - \mu \cdot \sin^2(1.27 \Delta m^2 L_{Near}/p_\mu)} \quad (21)$$

A sensitivity plot can be obtained by using p_μ (actually, the reconstructed muon momentum, $p_{\mu,rec}$) instead of E_ν . The result is shown in Fig. 52.

The sensitivity plot in Fig. 52 actually provides an “effective” sensitivity limit in the “effective” variables Δm^2 and $p_{\mu,rec}$. However, comparison between Fig. 51 and Fig. 52 demonstrates that the “effective” Δm^2 is simply scaled-off towards higher values, not affecting the mixing angle limit. The latter result is

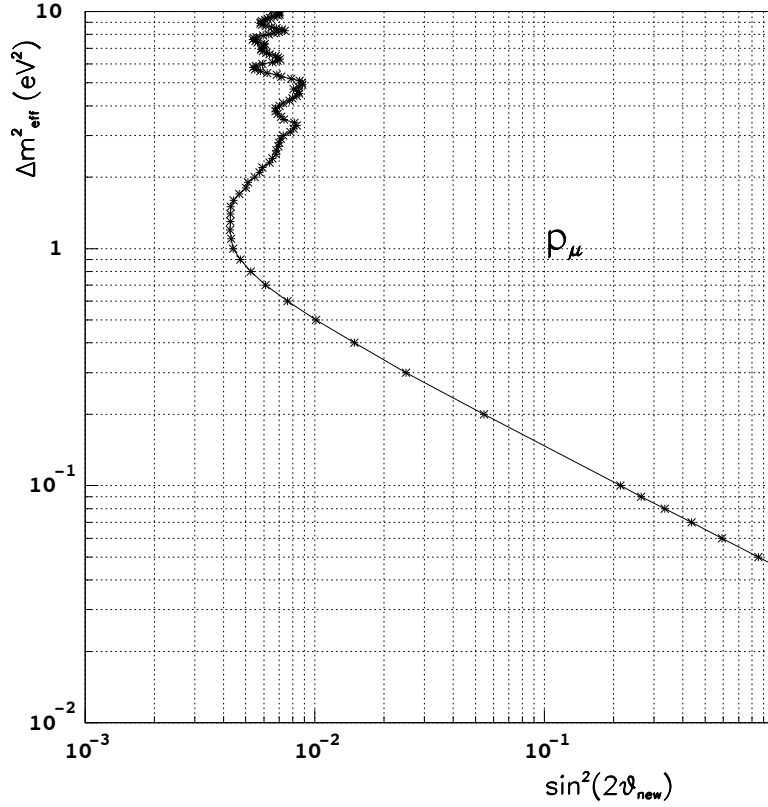


Figure 52: *The sensitivity plot obtained by computing the modified raster-scan method, in a CL_S framework, and by using the reconstructed muon momentum as estimator. A conservative cut of $p_{\mu, \text{rec}} \geq 500 \text{ MeV}$ has been applied.*

the best sensitivity that our experiment can achieve whether the systematics can be limited to 1% level, as we are confident in. A sensitivity to mixing angles in $\sin^2(2\theta_{\text{new}})$ below 10^{-2} can therefore be obtained in a large region of Δm^2 , around the 1 eV^2 scale.

13 Conclusions

Existing anomalies in the neutrino sector may hint to the existence of one or more additional *sterile* neutrino families. We performed a detailed study of the physics case in order to set a Short-Baseline experiment at the FNAL-Booster neutrino beam to exploit the measurement of the charged current events. An independent measurement on ν_μ , complementary to the already proposed experiments on ν_e , is mandatory to either prove or reject the existence of sterile neutrinos, even in case of null result for ν_e .

The already submitted proposals based on the technology of imaging in ultra-pure cryogenic Liquid Argon (LAr) may suffer from some experimental limitations, which we deem critical: the measurement of the muon charge on event-by-event basis extended to the lowest achievable momentum range would be needed. Moreover, very massive detectors are mandatory to collect a large number of events and therefore improve the disentangling of systematic effects.

The best option in terms of physics reach and funding constraints is provided by two spectrometers based on dipoles iron magnets, at the Near and Far sites (located at 110 and 710 m from the FNAL-Booster neutrino source, respectively), to be eventually placed behind the LAr detectors.

We plan to perform a full re-use of the OPERA spectrometers that will be started to be dismantled at the end of 2015. Each site at FNAL will host a part of the two coupled OPERA magnets, base on well know technology. The spectrometers will make use of RPC detectors, already available, which have demonstrated their robustness and effectiveness. The overall cost is two-fold: 1) the arrangement for the Near and Far sites, including servicing for assembling, is substantial but it may be part of a large SBL project at FNAL; 2) the overall cost of the experiment stays below 10 M€ and it can be largely covered by in-kind hardware. The remaining expenses can be shared between a large enough Collaboration.

We believe to have succeeded to develop a substantial proposal that, by keeping the systematic error at the level of $1 \div 2\%$ for the measurements of the ν_μ interactions, will allow in 3 years of data collection to:

- measure ν_μ disappearance in the almost entire available momentum range ($p_\mu \geq 500$ MeV). This is a key information in rejecting/observing the anomalies over the whole expected parameter space of sterile neutrino oscillations;
- measure the neutrino flux at the Near detector, in the relevant muon momentum range, which is decisive to keep the systematic errors at the lowest possible values;
- measure the sign of the muon charge to separate ν_μ from $\bar{\nu}_\mu$ to control systematics.

A sensitivity to mixing angles in $\sin^2(2\theta_{new})$ below 10^{-2} can be obtained in a large region of Δm_{new}^2 around the 1 eV^2 scale.

Acknowledgements

We are in debit to the FNAL and CERN managements for the encouragements towards the study of this proposal, in particular to Jim Strait and Sergio Bertolucci.

References

- [1] DAYA–BAY Collaboration, F. An et al., “*Observation of electron-antineutrino disappearance at Daya Bay*”, Phys. Rev.Lett. 108, 171803 (2012), arXiv:1203.1669.
- [2] RENO Collaboration, J. Ahn et al., “*Observation of Reactor Electron Antineutrino Disappearance in the RENO Experiment*”, Phys. Rev.Lett. 108, 191802 (2012), arXiv:1204.0626.
- [3] DOUBLE–CHOOZ Collaboration, Y. Abe et al., “*Indication of Reactor $\bar{\nu}_e$ Disappearance in the Double Chooz Experiment*”, Phys. Rev. Lett. 108, 131801 (2012), arXiv:1207.6632.
- [4] T2K Collaboration, K. Abe et al., “*Indication of Electron Neutrino Appearance from an Accelerator–produced Off–axis Muon Neutrino Beam*”, Phys. Rev.Lett. 107, 041801 (2011), arXiv:1106.2822.
- [5] B. Pontecorvo, Zh. Eksp. Teor. Fiz. 53, 1717 (1967) [Sov. Phys. JETP 26, 984 (1968)].
- [6] K.N. Abazajian et al., “*Light Sterile neutrinos: a White Paper*”, (2012), arXiv:1204.5379.
- [7] BICEP2 Collaboration, P. A. R. Ade et al., “*BICEP2 I: Detection Of B–mode Polarization at Degree Angular Scales*”, arXiv:1403.3985 [astro-ph.CO].
- [8] M. Archidiacono et al., “*Light sterile neutrinos after BICEP–2*”, arXiv:1404.1794 [astro-ph.CO].
- [9] J. Kopp, P. A. N. Machado, M. Maltoni, and T. Schwetz, “*Sterile neutrino oscillations: the global picture*”, JHEP 05, 050 (2013), arXiv:1303.3011;
T. Schwetz, “*Status of sterile neutrino oscillations*”, Nuclear Physics B, vol. 235-236, pp. 229235, 2013;
C. Giunti, M. Laveder, Y. F. Li, Q. Y. Liu, and H. W. Long, “*Update of short–baseline electron neutrino and antineutrino disappearance*”, Physical Review D, vol. 86, no. 11, Article ID 113014, 2012.
- [10] M. Netti et al., “*Letter of Intent for the new CERN Neutrino Facility (CENF)*”, <https://edms.cern.ch/nav/P:CERN-0000077383:V0/P:CERN-0000096728:V0/TAB3>.
- [11] MicroBooNE Experiment, <http://www-microboone.fnal.gov/>.

- [12] LAr1–ND Collaboration, C. Adams et al., “*LAr1-ND: Testing Neutrino Anomalies with Multiple LAr TPC Detectors at Fermilab*”, P–1053, 31 December 2013 and arXiv:1309.7987v3.
- [13] ICARUS Collaboration, M. Antonello et al., “*ICARUS at FNAL*” arXiv:1312.7252.
- [14] CDHS Collaboration, F. Dydak et al., “*A Search for ν_μ Oscillations in the Δm^2 range $0.3 \div 90 \text{ eV}^2$* ”, Phys. Lett. **B134**, 281 (1984).
- [15] MiniBooNE Collaboration, A. A. Aguilar–Arevalo et al., “*A search for muon neutrino and antineutrino disappearance in MiniBooNE*”, Phys. Rev. Lett. 103, 061802 (2009), arXiv:0903.2465.
- [16] MiniBooNE and SciBooNE Collaborations, K. B. M. Mahn et al., “*Dual baseline search for muon neutrino disappearance at $0.5 \text{ eV}^2 < \Delta m^2 < 40 \text{ eV}^2$* ”, Phys. Rev. D85, 032007 (2012), arXiv:1106.5685.
- [17] MiniBooNE and SciBooNE Collaborations, G. Cheng et al., “*Dual baseline search for muon antineutrino disappearance at $0.1 \text{ eV}^2 < \Delta m^2 < 100 \text{ eV}^2$* ”, Phys.Rev. D86, 052009 (2012), arXiv:1208.0322.
- [18] MINOS Collaboration, P. Adamson et al., “*Search for sterile neutrino mixing in the MINOS long–baseline experiment*”, Phys.Rev. D81, 052004 (2010), arXiv:1001.0336.
- [19] CCFR Collaboration, I. E. Stockdale and A. Bodek, F. Borcharding, N. Giokaris, K. Lang, K. et al, “*Limits on Muon Neutrino Oscillations in the Mass Range $55 \text{ eV}^2 < \Delta m^2 < 800 \text{ eV}^2$* ”, Phys.Rev.Lett. **52** 1384 (1984).
- [20] NESSiE Collaboration, P. Bernardini et al., “*Prospect for Charge Current Neutrino Interactions Measurements at the CERN–PS*”, SPSC–P–343 (2011), arXiv:1111.2242.
- [21] ICARUS and NESSiE Collaborations, M. Antonello et al., “*Search for anomalies from neutrino and anti–neutrino oscillations at $\Delta m^2 \sim 1 \text{ eV}^2$ with muon spectrometers and large LAr–TPC imaging detectors*”, SPSC–P–347 (2012), arXiv:1203.3432.
- [22] L. Stanco et al., “*An Appraisal of Muon Neutrino Disappearance at Short Baseline*”, AHEP 2013 (2013) ID 948626, arXiv:1306.3455v2.
- [23] The OPERA collaboration, R. Acquafredda et al. “*The OPERA experiment in the CERN to Gran Sasso neutrino beam*”, JINST **4** 4018 (2009).
- [24] J. R. Sanford and C. L. Wang (1967), BNL Internal Report, BNL–11479; MiniBooNE Collaboration, A. A. Aguilar–Arevalo et al., “*The Neutrino Flux prediction at MiniBooNE*”, 15 May 2009. arXiv:0806.1449v2, arXiv:hep–ex/0601022v1. 13 Jan. 2006.
- [25] S. E. Kopp., “*Neutrino spectra and uncertainties for MINOS*”, arXiv:hep–ex0712.1280. Dec. 2007.

- [26] G. Battistoni *et al.*, “*The FLUKA code: Description and Benchmarking*”, AIP Conf. Proc. **896**, 31 (2007).
- [27] C. Andreopoulos *et al.*, “*The GENIE Neutrino Monte Carlo Generator*”, Nucl. Instrum. Meth. **A614**, 87 (2010).
- [28] D. E. Groom, N. V. Mokhov, and S. Striganov,
<http://pdg.lbl.gov/2012/AtomicNuclearProperties/adndt.pdf>
- [29] [S. J. Barish *et al.*, “*Study of Neutrino Interactions in Hydrogen and Deuterium: Inelastic Charged Current Reactions*”, Phys. Rev. D **19**, 2521 (1979);
 N. J. Baker *et al.*, “*Total cross sections for ν_μ -n and ν_μ -p charged-current interactions in the 7-foot bubble chamber*”, Phys. Rev. D **25**, 617 (1982).
- [30] MINERvA Collaboration, FERMILAB-DESIGN-2006-01.
- [31] SciBooNE Collaboration, Y. Nakajima *et al.*, “*Measurement of inclusive charged current interactions on carbon in a few-GeV neutrino beam*”, Phys. Rev. D **83** (2011) 012005, arXiv:1011.2131.
- [32] SciBooNE Collaboration, Y. Kurimoto *et al.*, “*Measurement of Inclusive Neutral Current Neutral π^0 Production on Carbon in a Few-GeV Neutrino Beam*”, Phys. Rev. D **81** (2010) 033004, arXiv:0910.5768.
- [33] A. Bergnoli *et al.*, “*The OPERA Spectrometer Slow Control System*”, IEEE Trans. Nucl. Sci. **55** 349 (2008).
- [34] R. Santonico, R. Cardarelli, “*Development of Resistive Plate Counters*”, Nucl. Instr. and Meth. **A187** 377 (1981).
 R. Santonico, R. Cardarelli, “*Development of Resistive Plate Counters*”, Nucl. Instr. and Meth. **A263** 20 (1988).
- [35] P.K.F. Grieder “*Cosmic Rays at Earth*”, Elsevier (Amsterdam, 2011).
- [36] E. Balsamo, *et al.*, “*The OPERA RPCs front end electronics A novel application of LVDS line receiver as low cost discriminator*”, JINST **7** (2012) P11007.
- [37] G. J. Feldman and R. D. Cousins, “*Unified approach to the classical statistical analysis of small signals*”, Phys. Rev. D **57**, 3873 (1998),
<http://arxiv.org/abs/physics/9711021v2>.
- [38] http://www-boone.fnal.gov/for_physicists/data_release/flux/pospolarity_fluxes.dat.
- [39] B. Pontecorvo, Sov. Phys. JETP **26**, 984 (1968);
 Z. Maki, M. Nakagawa, and S. Sakata, Prog. Theor. Phys. **28**, 870 (1962).
- [40] W. Winter, “*Optimization of a Very Low Energy Neutrino Factory for the Disappearance Into Sterile Neutrinos*”, Phys. Rev. D **85**, 113005 (2012),
 arXiv:1204.2671.
- [41] <http://www.mpi-hd.mpg.de/personalhomes/globes/index.html>.
- [42] K. Mahn, *A search for muon neutrino and antineutrino disappearance with the Booster Neutrino Beam*, Columbia University 2009.

- [43] W. Huelsnitz, *Handling Uncertainties in IceCube with Covariance Matrices*, 26 April 2011.
- [44] C. Giunti, M. Laveder, Y.F. Li, H.W. Long, “*Pragmatic View of Short-Baseline Neutrino Oscillations*”, Phys.Rev. D88 (2013) 073008, arXiv:1308.5288.